Pliocene to Holocene deformation and earthquake potential of the Mesamávida fault, West Andean Thrust System of central-southern Chile (36ºS)

Vega-Ruiz, A.[1,2]; Cortés-Aranda, J.[3-4-11]; Aguilera-Cortés, R.[5]; Astudillo-Sotomayor, L.[6]; Riedel, M.[7]; Espinoza, M.[3-4;] Tassara, A.[3]; Nelson, A.[8]; Melnick, D.[9]; Lupi, M.[10]; Arriagada, D.[3]; Sepúlveda, T.[3]; Álvarez-Amado, F.[3-4-12]; Navarro, L[7].

[1] German Research Center for Geosciences (GFZ), Germany

[2] Institute for Geological Sciences, Freie Universität Berlin, Germany

[3] Departamento Ciencias de la Tierra, Facultad de Ciencias Químicas, Universidad de Concepción, Chile

[4] Anillo Project SALARES

[5] Institut des Sciences de la Terre (ISTerre), France

[6] Escuela de Ciencias del Mar, Pontificia Universidad Católica de Valparaíso, Chile

[7] Doctorado en Ciencias Geológicas, Universidad de Concepción, Chile

[8] United States Geological Survey (Emeritus), Golden, Colorado, United States

[9] Instituto de Ciencias de la Tierra, Universidad Austral, Chile

[10] University of Geneva. Switzerland

[11] CIMASur Interdisciplinary Group, Universidad de Concepción, Chile

[12] Water Research Center for Agriculture and Mining - CRHIAM, ANID FONDAP Center, Concepción, Chile.

Corresponding author: Joaquín Cortés-Aranda (joacortes@udec.cl)

Key Points:

- The Western Andean Thrust System (WATS) has shaped the Valley-Principal Cordillera limit at 36°S since the Pliocene.
- Late Pleistocene to Holocene deformation in the WATS at 36°S is marked by the scarp of the Mesamávida fault, a NNE-striking reverse fault.
- The Mesamávida fault has produced magnitude 5.56 to 7.06 earthquakes during the Holocene and is a significant seismic hazard.

Abstract

Crustal reverse faults are recognized for their potential to generate devastating earthquakes, making them a focus of seismic hazard assessment. Along the Chilean Andes, the Western Andean Thrust System (WATS)—a structure marking the Central Valley-Principal Cordillera border—includes several probable late Quaternary faults. However, evidence for large Holocene earthquakes (M~7) has only been confirmed on two faults at ~32-33°S. This study focuses on the WATS at ~36°S, where a hectometer-scale escarpment dominates the border between the Central Valley and Principal Cordillera. LiDAR-derived topography, new geologic mapping of Pliocene to Quaternary units, and morphological analysis reveal that the mountain front and surrounding areas have undergone tectonic deformation since at least the Pliocene. Approximately 200 m west of the mountain front, we mapped a 0.7-to-8.7-m-high fault scarp in alluvial deposits dated at ~14 ka with Optically Stimulated Luminescence (OSL). Morphotectonic analysis of the scarp and faults mapped in two trenches demonstrates that the scarp formed during moderate to large Holocene earthquakes along the newly identified Mesamávida fault. A local seismic network also detected crustal seismicity likely attributable to the fault. At least one branch fault of the WATS at 36°S—the Mesamávida fault—has the potential to generate earthquakes with magnitudes up to ~7.1. The seismic potential of the Mesamávida fault should be incorporated into hazard analyses for central-southern Chile. Study of similar faults within the WATS to the north and south will enhance understanding of this thrust system's seismic hazard and its role in Quaternary tectonics of the Andes.

Plain Language Summary

Movement of crustal reverse faults, where a shallow slice of Earth's crust is pushed over another, can cause powerful earthquakes, making them crucial for hazard assessment. In the Chilean Andes, the Western Andean Thrust System (WATS) lies between the Central Valley and Principal Cordillera, including several faults that may have produced large earthquakes in the past 100,000 years. So far, evidence for large earthquakes in the past 10,000 years has only been confirmed on two faults at ~33°S. We investigated the WATS at 36°S, where a steep mountain front shows signs of tectonic activity since ~2.5 million years ago. Near the front, we discovered a 0.7-to-8.7-m-high scarp in alluvial sediments. By dating these sediments, studying faults in two trenches across the scarp, and analyzing its shape, we found that the scarp formed during at least two earthquakes in the past 10,000 years as large as magnitude ~7.1. Instruments record tiny earthquakes nearby the fault nowadays. Hence, the Mesamávida fault is an active structure with the potential for similar future earthquakes and must be included in seismic hazard analyses for the region. Further studies north and south will improve understanding of the seismic hazard posed by WATS faults in central Chile.

1. Introduction

Compressional crustal faults are a significant source of seismic hazard that can host damaging earthquakes (e.g., Anderlini et al., 2020; McCalpin, 2009; Stein & Yeats, 1989; Yang et al., 2021). Destructive strong events include the recent 2019 M6.4 Albania earthquake (Teloni et al., 2021) and the 2023 M6.9 Morocco earthquake (transpressive, Cheloni et al., 2024), while larger destructive events include the 1999 M7.7 Chi-Chi earthquake (Uzarski & Arnold, 2001), the 2005 M7.6 Kashmir earthquake (Pathier et al., 2006), and the 2008 M7.9 Sichuan earthquake (Burchfiel et al., 2008). Despite their destructive capacity, geomorphic and stratigraphic evidence of slip on these faults, even during the largest prehistoric shallow compressional earthquakes, events (~M7-8 and depths <10 km), is commonly subtle, difficult to identify, and even more challenging to date (e.g. Marliyani et al., 2016; McCalpin, 2009; McCalpin et al., 2023). Consequently, the seismic hazard from compressional faults is frequently underestimated.

In the central-southern Andes between 31°S and 38°S, the Quaternary to present-day shortening induced by Nazca-South America plate convergence is primarily accommodated in the upper plate along the eastern Andean slope by N-S striking thrust faults (Costa et al., 2000; Kendrick et al., 2006; Rockwell et al., 2014; Schoenbohm et al., 2013; Zapata & Allmendinger, 1996). Some of these faults have produced large earthquakes, such as the Laja fault (31.5ºS), a NE-striking and west-verging structure that caused the 1944 M7 San Juan earthquake, one of the most destructive earthquakes to have struck Argentina (Alvarado & Beck, 2006; Rockwell et al., 2014). In contrast, Quaternary shortening on the western Andean flank in Chile has been documented at only two locations near the Central Valley-Principal Cordillera boundary along branches of the West Andean Thrust System (WATS) (e.g., Armijo et al., 2010; Estay et al., 2023, Fig. 1a). The San Ramón fault at 33.5°S is a seismogenic west-verging thrust ramp (Armijo et al., 2010). This fault has produced two M~7.5 earthquakes over the past 19 ka, the last occurring about 8 ka (Vargas et al., 2014) and it could rupture in a large earthquake in the near future. Estay et al. (2016) and Ammirati et al. (2019) consider instrumental seismicity along the San Ramón fault as additional evidence supporting the significant seismic hazard posed by the fault for urban areas in the region. Further north (32.8°S), Estay et al. (2023) document thrusting of late-Cenozoic rocks over Quaternary alluvial deposits along the Cariño Botado fault, a west-verging reverse fault. Fault segments of 5 to 15 km long on the main trace of the Cariño Botado fault show ~4.9 m of slip during the past 8.7 ka. Based on the fault's length and slip, earthquakes M ≤7.5 can be expected on the Cariño Botado fault (Estay et al., 2023). No moderate to large historical compressive earthquakes have occurred along the WATS yet. The absence of studies of the potential for large earthquakes north and south of the San Ramón and Cariño Botado faults along the WATS has left critical gaps in our understanding of seismic hazard for the many population centers and industrial facilities of the Central Valley of Chile (Fig. 1a).

This study focuses on the Central Valley-Principal Cordillera boundary at 36°S in the Maule Region near the town of Mesamávida (Figs. 1b & 2a). Here, the boundary area features a steep (~17°) mountain front in Neogene units (black/yellow line in Fig. 2a). Based on a 1-to-5-m-resolution LiDAR DTM (Digital Terrain Model) of the area, new geologic mapping of Pliocene to Quaternary units, and morphological analysis, we argue that the mountain front and surrounding areas have undergone tectonic deformation along a branch fault of the WATS since at least the Pliocene. Running parallel to and west of the mountain front lies the herein named Mesamávida scarp, formed in late Quaternary alluvial deposits (red line in Figs. 2a & 3). Based on optically stimulated luminescence (OSL) dating of the alluvial deposits, detailed investigation of two trenches across the Mesamávida scarp, and morphotectonic analyses of the scarp, we demonstrate that this feature was produced by Late Pleistocene-Holocene (<14 ka) surface faulting along the Mesamávida fault. With a local seismic network, we also recorded crustal microseismicity likely attributable to the fault. Our findings confirm that the Mesamávida fault has generated surface-rupturing earthquakes as large as M~7.1 during the late Pleistocene-Holocene and has the potential for similar future events. Consequently, the fault poses a substantial seismic hazard for the over one million residents and critical infrastructure of the Maule Region.

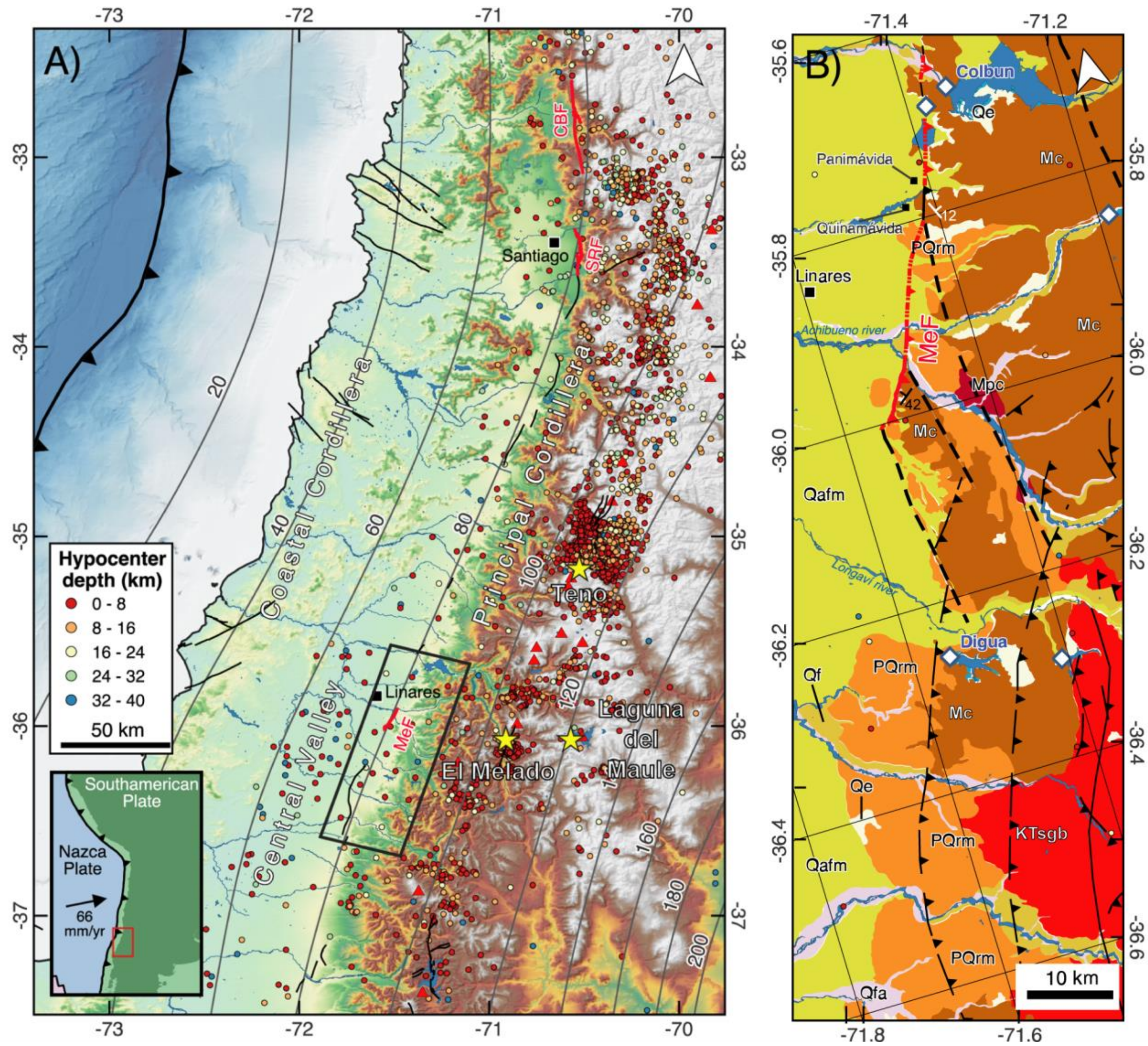

Figure 1. Tectonic overview of Central Chile and geologic setting of the study area. **(a)** Shaded relief map of central-southern Chile showing the main morphostructural units (see inset for location). Black rectangle shows the study area in (b). Faults of the Chilean Active Faults database (Maldonado et al., 2021) are represented by black lines; the San Ramón (SRF, Vargas et al., 2014), Cariño Botado (CBF, Estay et al., 2023), and Mesamávida (MeF) faults are depicted by thick red lines; these faults are active branches of the West Andean Thrust System. Instrumentally recorded earthquakes for the Central Valley and Principal Cordillera (≤40 km depth) are marked by colored circles (NSF SAGE and OVDAS databases). Yellow stars mark three shallow M >6 earthquakes near the study area. Red triangles are active volcanoes. **(b)** Simplified geologic map for the Central Valley-Principal Cordillera area between 35.5°S and 36.5°S. Lithologic units from Karzulovic & Hauser (1979); mapped structures from Hauser (1995) and Muñoz & Niemeyer (1984). KTsgb: granitic rocks of the Tertiary Santa Gertrudis-Bullileo batholith; Mc: Miocene Colbún Formation; Mpc: Miocene Campanario Formation; PQrm: Pliocene to Quaternary "Rodados multicolores" unit; Qafm, Qf, Qe, and Qfa, are Quaternary alluvial deposits. Dams are located with white diamonds.

2. Geological and seismotectonic background

Between 35.8°S and 36.5°S, the Central Valley-Principal Cordillera boundary trends NNE (Figs. 1 & 2a). South of 36ºS, the boundary is dominated by a distinct, hectometer-scale mountain front; to the north, the boundary contains inselbergs contributing to the irregularity of the boundary (Oviedo-Reyes et al., 2024). The main geological units exposed between the given latitudes have been mapped and characterized by Hauser (1995), Muñoz & Niemeyer (1984) and Karzulovic & Hauser (1979) (Figs. 1b & 2a).

The oldest rocks in the area outcrop south of 36.2ºS and correspond to the Upper Cretaceous-Lower Miocene Santa Gertrudis-Bullileo Batolite (KTsgb, Spikings et al., 2008) (Fig. 1b). This unit consists of monzogranite to quartziferous diorite (Muñoz & Niemeyer, 1984). To the west and north, the Colbún Formation (Mc) is exposed, comprising Oligocene-Miocene volcanic and sedimentary successions (Figs. 1b & 2a, Karzulovic & Hauser, 1979; Vergara et al., 1999). Along the Achibueno River, pyroclastic and sedimentary rocks of the Colbún Formation are intruded by grey-green andesitic porphyry hypabyssal rocks (Mpc in Fig. 1b).

The larger valleys in the study area have accumulated several generations of Pliocene to Quaternary fluvial-alluvial deposits (Figs. 1b & 2a; Hauser, 1995). Along the northern side of the Achibueno River valley, and occasionally within the Central Valley, the Rodados Multicolores unit (PQrm in Figs. 1b & 2a; Hauser, 1995) outcrops. This unit includes massive to gently imbricated Pliocene-Quaternary polymictic conglomerates with ~15-cm-diameter andesitic and granitic clasts in a discontinuous sandy matrix. A distinctive feature of this unit is the orange alteration exhibited by its clasts (Hauser, 1995). Younger unconsolidated deposits of abandoned fluvial-alluvial plains within the Central Valley are mapped as the Ancoa-Achibueno Fan (Qafm in Figs. 1b & 2a; Hauser, 1995), primarily composed of conglomerates with discontinuous sand beds. Several generations of younger unconsolidated deposits are labeled, from older to younger, Qf, Qe, and Qfa units. The Qf unit consists of gravel with sand beds in abandoned terraces (Figs. 1b & 2a). The Qe unit consists of massive alluvial deposits with clasts of heterogeneous size, shape, and composition, in a discontinuous muddy-sand matrix (Fig. 2a); and the Qfa unit corresponds to gravel and sandy gravel occupying the modern floodplains of the main rivers in the area (Fig. 1b; Hauser, 1995).

Although no structures have been previously documented near the Mesamávida fault (36°S, Fig. 1b), Hauser (1995) and Vergara et al. (1999) report NS striking faults at ~35.7°S in pre-Quaternary rock units, coherent with the structural pattern in longitudinally equivalent areas of central Chile (Fig. 1b). Near the Colbún Dam (Fig.1b), Hauser (1995) indicates that breccias exhibit fractures and faults with varying dip angles and orientations, including N40°-80°E, E-W, and N10°E. He also links the thermal activityy observed at Panimávida and Quinamávida springs (Fig. 1b) to a regional NNE striking fault. This latter structure is depicted in the geological map by Contreras et al. (2024), who, based on field observations and preliminary research on the Mesamávida fault at 36ºS (Sepúlveda et al., 2018; Arriagada et al., 2022), propose that it extends northward to the vicinity of the Colbún Dam (35.6ºS; Fig. 1b). Additionally, Espinoza et al. (2024), using gravimetric and magnetotelluric profiles, support the presence of a structure—interpreted as the Mesamávida fault—along the boundary between the Central Valley and the Western Cordillera, between 35.6ºS and 36ºS. Between 36.1°S and 36.4°S, Radic (2010) interprets NNE-striking, east-dipping faults as drivers of compression and basin inversion since the Late Miocene (Fig. 1b). At 37°S, Rojas Vera et al. (2014) map dominantly west-verging reverse faults resulting from tectonic inversion of the Cura-Mallín Basin (Radic, 2010), suggesting that these faults root in a regional detachment at ~16 km depth. A frontal fault on the western Andean slope's west edge may drive Mesozoic deformation to Miocene units in this region (Rojas Vera et al., 2014).

Global seismic catalogs show sparse earthquake activity in the Central Valley and Principal Cordillera between 35°S and 37°S (Fig. 1). Fig. 1a displays all crustal earthquakes (depths ≤40 km) included in the NSF SAGE catalog (ds.iris.edu/ds/nodes/dmc/data/types/events/catalogs/) between 1975 and 2022, along with locations from the OVDAS catalog (Southern Andes Volcanological Observatory, rnvv.sernageomin.cl/observatorio-volcanologico-de-los-andes-del-sur/). The NSF SAGE catalog in our study area is formed by events reported by the USGS NEIC-PDE and the ISC global catalogs. It is therefore limited to moderate-to-large events (M>4) with relatively large location errors (~10 km). The OVDAS catalog is produced from a seismic network dedicated to monitor active volcanoes and therefore is relatively accurate near the volcanic arc (location errors <5 km), but with larger uncertainties far from them. It contains smaller events than global catalogs, down to Ml –0.7, but low magnitude detections are limited to volcanic edifices. Although shallow earthquakes are not concentrated along the mountain front, the reported seismicity shows some events distributed throughout the area. North of the study area (Fig. 1a), in the Principal Cordillera at 34.9°S, the M6.7 2004 Teno earthquake nucleated at 4.7 km depth, likely along the NE-striking dextral El Fierro fault (Comte et al., 2008). A M6.2 earthquake, also in the Principal Cordillera at 36ºS (Fig. 1a), is probably linked to the NNE striking dextral El Melado fault (e.g., Cardona et al., 2018; Lupi & Miller, 2014)The catalog also documents an M6 earthquake at ~8 km depth in the Laguna del Maule area.

3. Tectonic geomorphology of the Central Valley-Principal Cordillera boundary

We analyze the morphology of the Central Valley-Principal Cordillera boundary near 36°S using a 1-to-5-m-resolution LIDAR DTM (provided by the Arauco Forestry Company; https://arauco.com/chile/; Fig. 2). Four swath profiles (500-1000 m wide) across the DTM and field observations shed light on the Pliocene to Quaternary response of this landscape to tectonics (Fig. 2a; Schwanghart & Scherler, 2014). Profile I-I’ crosses a scarp formed in PQrm deposits north of the Achibueno River valley (Figs. 2a & 2d); profile II-II’ follows the strike of the mountain front (Fig. 2e); profile III-III’ crosses the main mountain front (Fig. 2f); and profile IV-IV’ follows the NNE elongation of the Mesamávida hill (Fig. 2g).

A ~8-km-long NNE-striking mountain front dominates the Central Valley-Principal Cordillera boundary at ~36°S (Fig. 2a). The mountain front is truncated to the south by the late Quaternary floodplain of the Longaví River and to the north by the Achibueno River (Figs 2a & 3a). The mountain front’s elevation progressively increases northwards from ~50 m to ~120 m between the mentioned rivers. The across-strike swath profile in Fig. 2f illustrates that the mountain front is very steep (~17°). Furthermore, a west-dipping surface is preserved over the Mc unit to the east, and a flat surface developed over Qafm and Qe deposits to the west. In the area covered by Fig. 2a, we have characterized unit Qe in road crosscuts (Fig. 4c); outcrops expose sections up to 20 m in height of massive matrix-supported and poorly selected alluvial gravels. Clasts are subrounded and range in size between a few centimeters and 0.5m; the matrix is sandy and contains fragments of undifferentiated lithics and quartz. Sand lenses up to 3 m long and 0.5 m wide were observed (Fig. 4c-d). Qe deposits in the area occur as cones connected to active channels and not extending more than 1000 m westward the mountain front; they cover Qafm deposits westward and overlap the Mc unit immediately east of the mountain front (Fig. 2a). Mc beds dip 42NW° southwards of the Achibueno River, while they are mostly subhorizontal along the mountain front northwards of the Achibueno River at 35.8ºS (Fig. 1b). Although no faults are mapped at this portion of the mountain front, ~5 km to the east, we mapped a NNE-striking and east-dipping fault ─ likely reverse (Figs. 2a-b). This fault forms a 20-m-high scarp in unit PQrm 170 m above the Achibueno River (Figs. 2d).

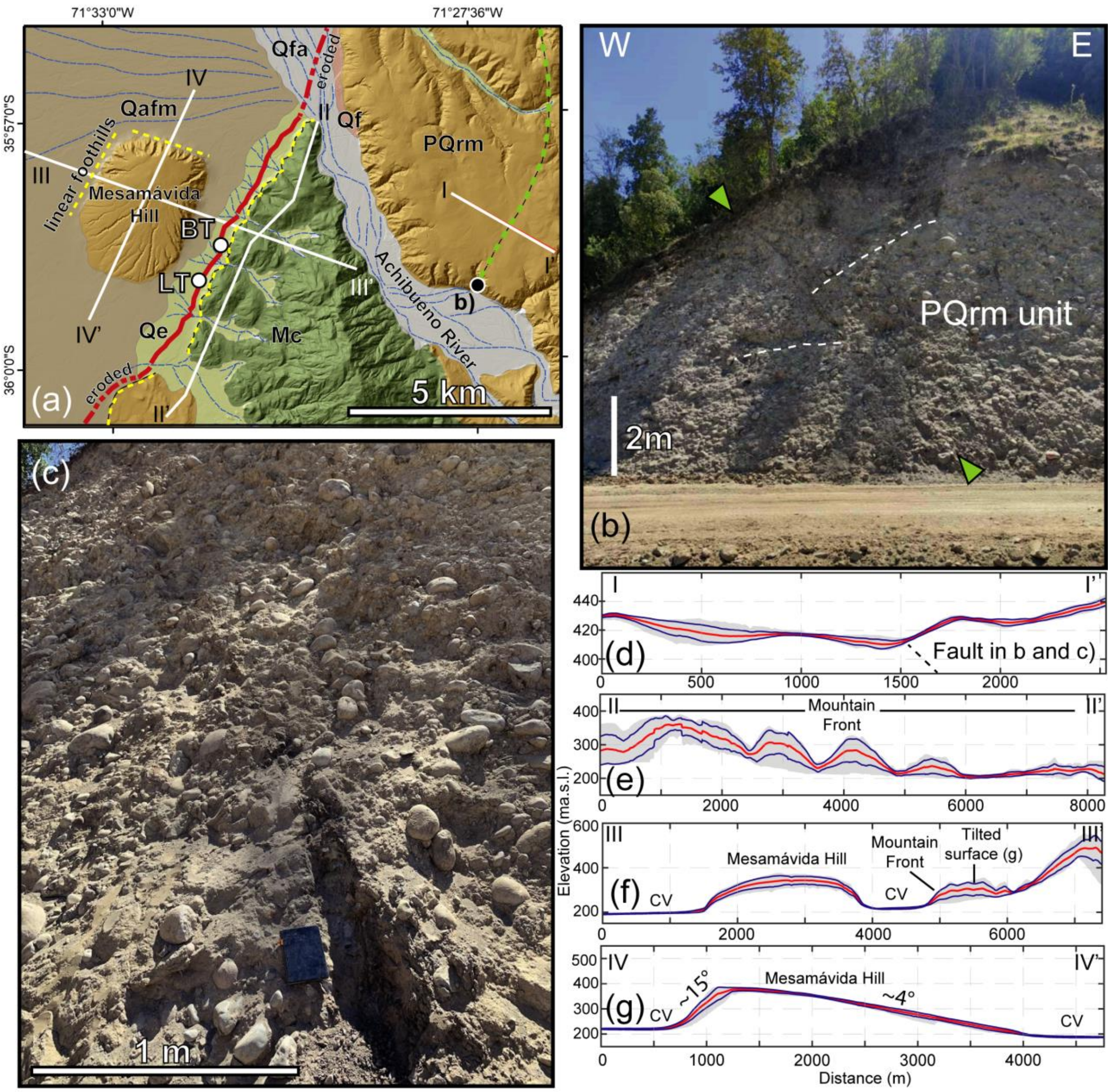

Figure 2. Geologic and geomorphologic features of the Central Valley-Principal Cordillera boundary within the study area. **(a)** Geology near the Mesamávida scarp. Geologic units as in Fig. 1b. White lines mark the location of profiles shown in (c-f). Thick black & yellow is the mountain front. The red continous and dashed lines are the Mesamávida scarp and its suspected eroded continuation, respectively. Black circle shows location of photo in (b); white circle marks location of trenches (BT= Barros Trench; LT = Lupe Trench). Note the SW dip of Mc units eastwards of the mountain front. **(b)** Photograph showing north-facing exposure of a reverse fault north of the Achibueno River. Green arrows mark the trace of the fault; dashed lines locate an apparent displaced bed. **(c)** Close-up view of the fault shown in (b). **(d- g)** topographic profiles in the study area (located in a). Note the west dipping surface in (f). Profile (g) shows the southwestward inclination of the Cerro Mesamávida. Red lines indicate the mean topography, grey zones (bounded by blue lines) show 1 standard deviation errors on the mean topography. Swath widths are 500 m for I-I' and 1000 m for the other profiles. CV: Central Valley.

About 800 m west of the mountain front, the Mesamávida hill is an anomalous NNE-elongated landform of the eastern Central Valley (Figs. 1b, 2a & 3a). The 3.5-km-long and 2.6-km-wide hill has linear eastern and western edges and presents steeper north and east slopes (Figs. 2a & 2g). A piedmont area between the mountain front and the Mesamávida hill is characterized by unit Qe overlying unit Qafm (Fig. 2a); our mapping differs from that of Hauser (1995), who does not show unit Qe crossing the mountain front (Fig. 1b).

A NNE-striking fault scarp is built in alluvial deposits of unit Qe between the Achibueno and Longaví rivers and is eroded across the valleys of the same rivers (red line in Figs. 2a & 3). This scarp, herein called Mesamávida scarp, is ~8 km long and its height ranges from 0.7 to 8.7 m. At ~200 m east of the Mesamávida scarp, we obtained an OSL age of 14.2 ± 1.7 ka for a sand lens interbedded in gravels from unit Qe (Figs. 3b & 4c, Supplementary Information 1). Three reasons suggest that the age is accurate: (1) the dated quartz grains gave a good luminescence response used in constructing a calibration curve; (2) a recycling test was used to verify that the OSL response remained consistent (<10% variation) despite the many environmental processes the sample was probably subjected to since it was deposited, and (3) a recuperation test signal designed to check for deep traps in samples by measuring a zero-dose signal varied <10% (Supporting Information 1). We use this age to infer a late Pleistocene age for the alluvial deposits in which the Mesamávida scarp is developed.

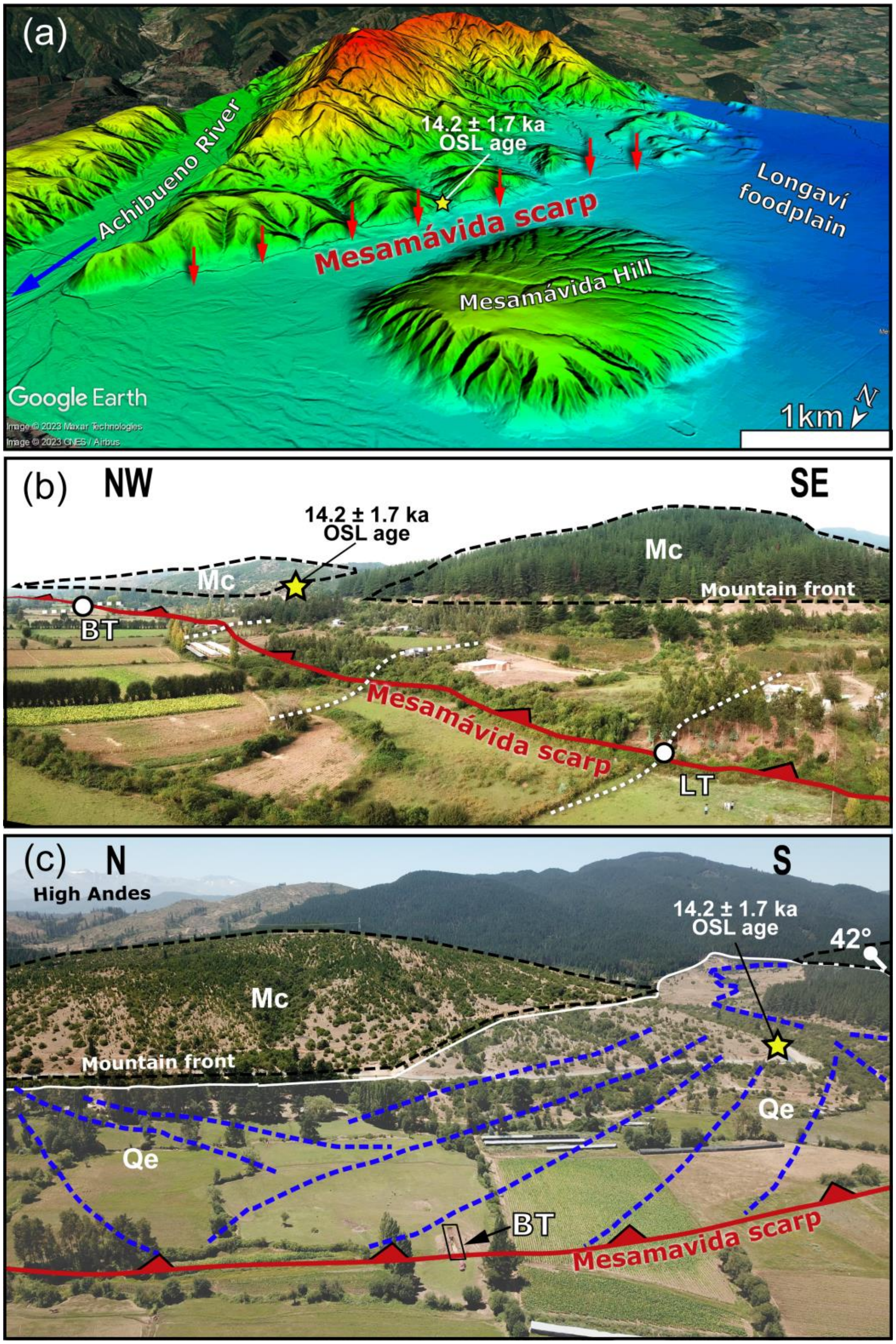

Figure 3. Overview of the Mesamávida scarp and OSL sample location **(a)** Inclined view of the Mesamávida scarp from the northwest. Red arrows mark the scarp at the base of the piedmont west of the mountain front. Yellow star depicts the OSL age location. **(b)** Drone view towards northeast of the Mesamávida scarp; red line traces the scarp base at the location of the scarp trench sites (white dots; BT = Barros Trench; LT = Lupe Trench); white dashed lines denote the shape and height of the scarp at four places along its trace. **(c)** Drone view towards the east of the Mesamávida scarp; a light-colored area with dashed blue lines is a massive alluvial fan in which the scarp formed (Qe).

4. Stratigraphic evidence of surface faulting along the Mesamávida fault scarp

To confirm a surface-faulting origin for the scarp, we excavated two trenches perpendicular to its central section: the more southerly Lupe trench (LT, 14.6 m long, 3 m wide and 4 m deep) and the Barros trench (BT, 20 m long, 2.25 m wide and 3 m deep) 1 km to the north (Figs. 2a & 5-10). At these sites, vertical offsets of the scarp are ~6.22 m and ~2.74 m, respectively (Fig. 4). The shallow water table at the trench sites limited them to ~12 m long with maximum depths of ~3.5m.

We mapped the stratigraphy and structure of the northern walls of the trenches on photomosaics composed of hundreds of photographs with 75% overlap (structure-from-motion methods of Reitman et al., 2015). We based the description of the stratigraphic units in the unconsolidated coarse-grained sediment on variations in colour, matrix, size, and distribution of clasts (Kübler et al., 2018; McCalpin, 2009; McCalpin et al., 2023; Rockwell et al., 2009; Vargas et al., 2014). Both trenches expose alluvial gravel deposits of unit Qe and scarp colluvium derived from them (Figs. 5-6 & 8-9); gravel units include subrounded and polymictic clasts mainly of andesitic and granitic rocks. We focused on identifying faults and fault zones with offset gravel beds and rotated clasts and estimating the displacement along them. No organic materials for radiocarbon dating were found in the trenches; the water content of a sand lens in the Barros Trench (Fig. 4d) precluded its dating by OSL. To validate our interpretation of the deformation histories of each trench, we used geometrical forward modelling (MOVE Software; PE Limited, 2020) to make palinpastic restorations of each trench wall log.

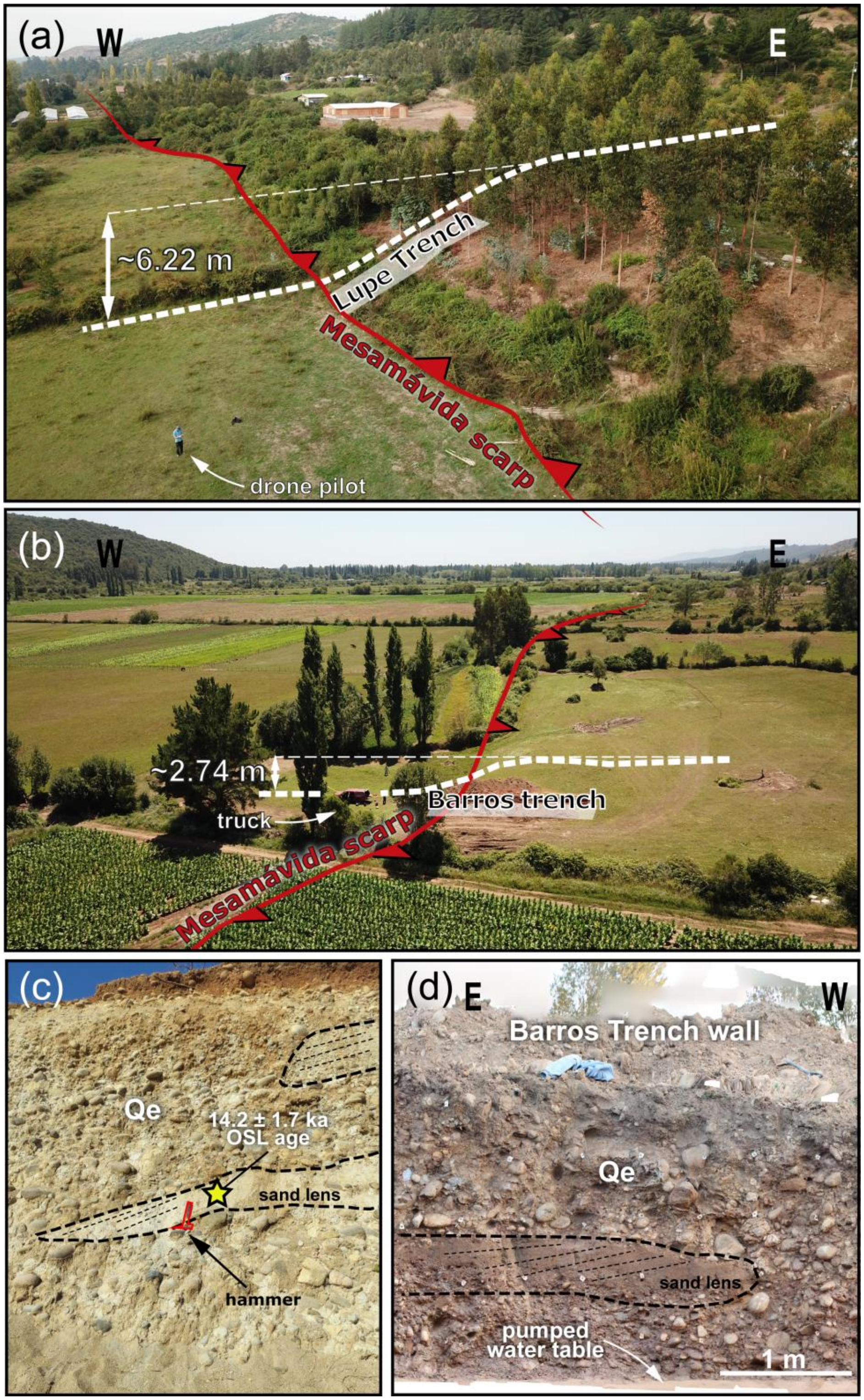

Figure 4. Overview of paleoseismic trenches location and observed Qe deposits. **(a-b)** Drone view of the Mesamávida scarp at the Lupe and Barros trench sites, respectively. Red lines trace the scarp base, white dashed lines denote the shape and height of the Mesamávida scarp at each site. **(c)** Outcrop of alluvial deposits (Qe) containing the sand lens, which could not be dated. Location in Fig. 3. **(d)** Deposits and sand lenses of Qe in the Barros trench wall.

4.1. Lupe Trench

Mapped units in the north wall of the Lupe trench are labelled A to E from older to younger (Fig. 5). At the base of the trench wall, Unit A is a coarse-grained gravel (>1.4 m thick, ~30% gravel matrix). This unit is moderately sorted with weak stratification marked by cobbles and boulders (Fig. 5c). Unit B is a fine-grained pebble gravel (0.6 m thick, ~15% matrix), with well-defined stratification (Fig. 5c); its contact with unit A is irregular. Unit C is a chaotic, matrix-supported (~35%) and extremely poorly sorted (pebbles to boulders) wedge-shaped gravel of 1-1.5 m thick, which we infer to be a colluvium. Its contact with unit B is erosive, and its upper contact with unit D is irregular. Unit D is a 0.3-m-thick, matrix-supported (~45%) pebble gravel. Its matrix has a subangular blocky structure, suggesting the development of a B soil horizon. Overlying unit E is a 0.25-m-thick matrix-supported (~45%) gravel with scarce pebbles; its matrix is granular, dark colored, and organic-rich, corresponding to a modern A soil horizon of the alluvial surface. Its lower contact with unit D is predominantly planar.

In the center of the trench wall, we mapped a subtle, east-dipping (~40ºE), NNE-striking, and ~0.35 m wide reverse fault zone. This fault zone contains fine-grained sediment and abundant rotated and fractured clasts (Fig. 5 & 6). All stratigraphic units are truncated by the fault zone (Fig. 5c-d). Units A and B are folded close to the fault zone, forming a hanging wall anticline. Minor fractures are observed in units B to D in the footwall of the fault zone (red segmented lines in Fig. 5).

The position of the fault zone and offset of all alluvial units and colluvial deposit in the Lupe trench wall shows that the Mesamávida scarp is the product of Late Pleistocene to Holocene reverse surface-faulting during a single or a series of earthquakes (Fig. 5c). A subtle slope break occurs on the scarp directly above the fault zone, supporting a young age for faulting (Fig. 5a). Thus, it is possible to interpret Unit C as a colluvium deposit likely formed by collapse of the upper scarp following surface rupture. The main markers along the fault zone are the top of unit B, offset by ~0.86 m, and the contact between units D and E, offset by ~0.2 m (Fig. 5c). Based on the offsets and the fact that Unit C hanging-wall-collapse coluvium is faulted, we identified two faulting events that we attribute to paleoearthquakes. During the first event, the fault slipped ~0.66 m and displaced Unit A and B. Before the second event, part of the hanging wall collapsed, forming the colluvial deposit Unit C. Then, Unit D was deposited, and soil was developed in it. During the second event, the same fault slipped ~0.2 m and displaced units A to E.

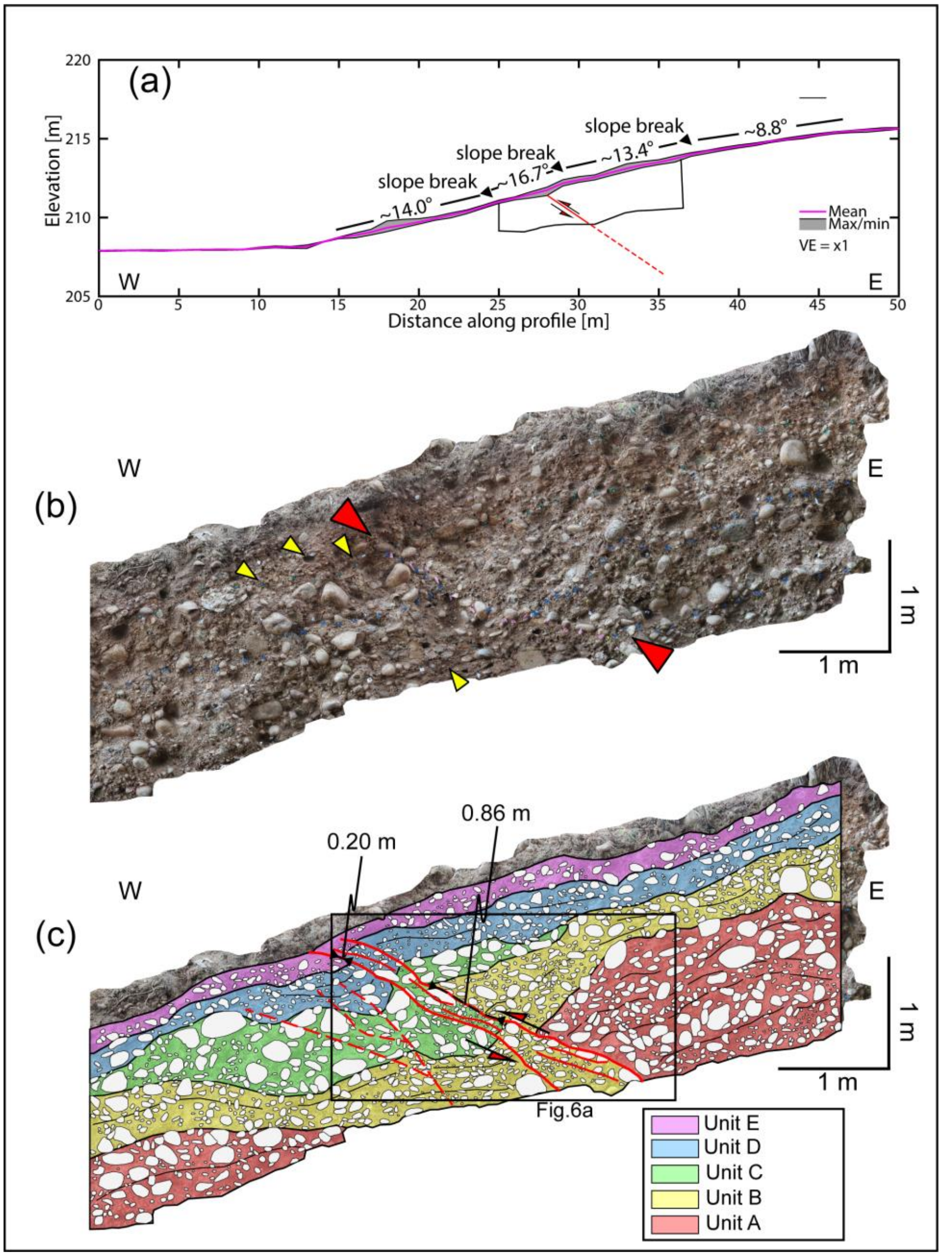

Figure 5. Logging of the Lupe trench. **(a)** Topographic swath profile at the trench site (5 m wide). The black line depicts the excavation, and the red line is the fault trace. Note the slope break**s** along the profile where the fault **zone** reaches the surface. **(b)** Photomosaic of the northern wall of the trench. Red and yellow triangles indicate end points of the trace of the main fault zone and related fractures**, respectively**. **(c)** Mapped trench wall with labeled units (described in the text); solid and dashed red lines mark the faults and fractures**,** respectively. The rectangle shows the area shown in Figs. 6a-b.

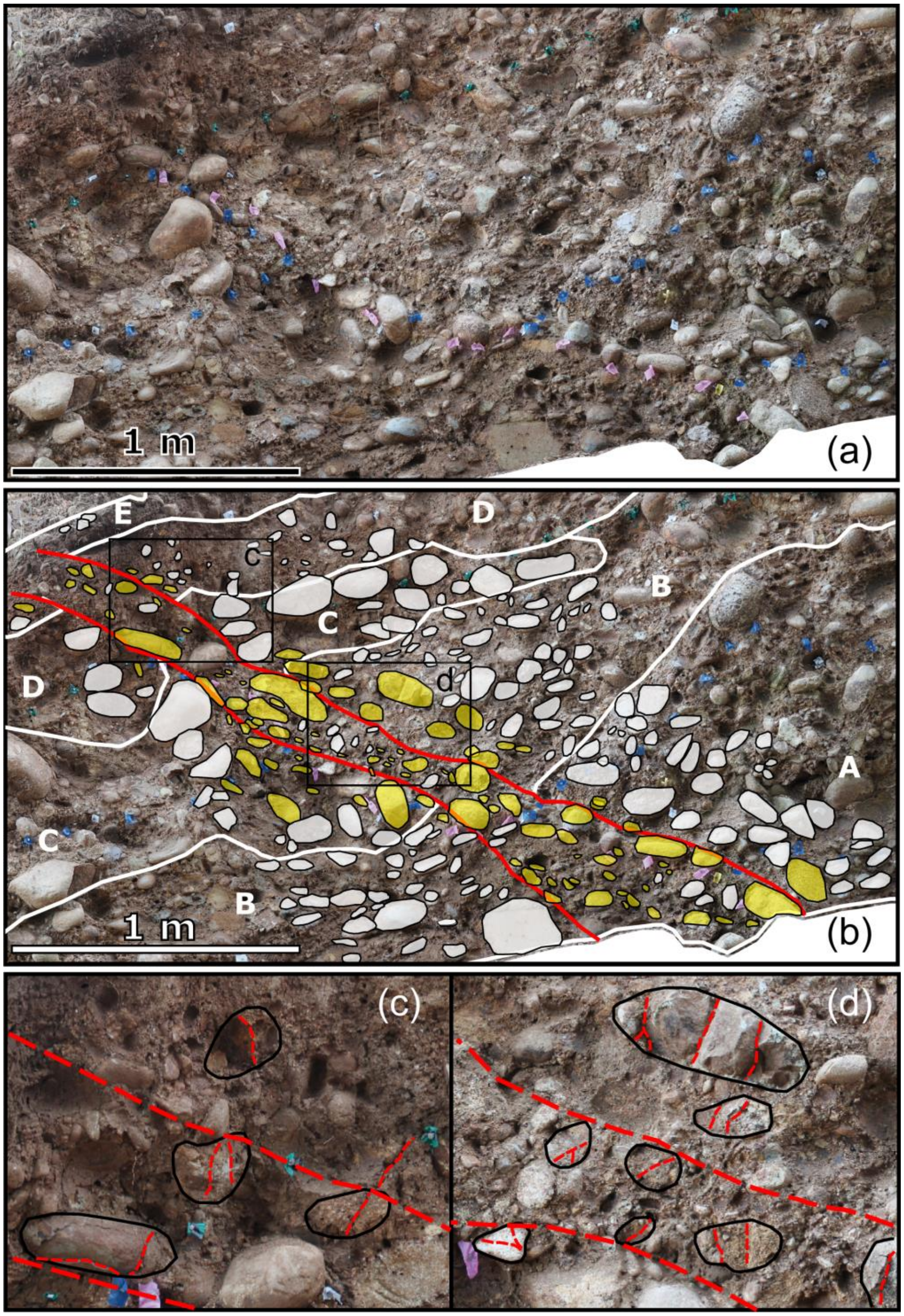

Figure 6. Close-up to the fault zone mapped in Lupe trench. **(a- b)** Unlabeled and labeled close-ups of the fault zone in the trench wall. Yellow-colored clasts correspond to rotated clasts within and close to the fault zone. **(c-d)** Fractured clasts within and close to the fault zone, fractures highlighted by thin dashed red lines; thicker red lines delineate edges of the fault zone characterized by fine-grained sediment.

Based on the geometry of the hanging wall anticline and the displaced contact offsets, we modeled the deformation as the result of multibend, fault-bend folding during two earthquakes (Medwedeff & Suppe, 1997) (Fig. 7). In this forward geometrical modelling, we propose a faulting history starting with subhorizontal, slightly west-dipping gravel units in the trench (Fig. 7a). A reverse fault similar to that in the trench accommodates a first slip event of 1.4 m, deforming units A and B (Fig. 7b). This generates a scarp which subsequently collapses, forming colluvium in its lower part (unit C; Fig.7c). The colluvium, along with the entire scarp, is then covered by deposition of alluvial gravels of units D (Fig. 7c) and E (Fig. 7d). A second slip event on the fault of 0.2 m then further deformed the gravel units (Fig. 7d), resulting in the stratigraphy as mapped in the trench. During each modeled slip event, folding is imprinted on the eastern fault block, resulting in a hanging wall anticline.

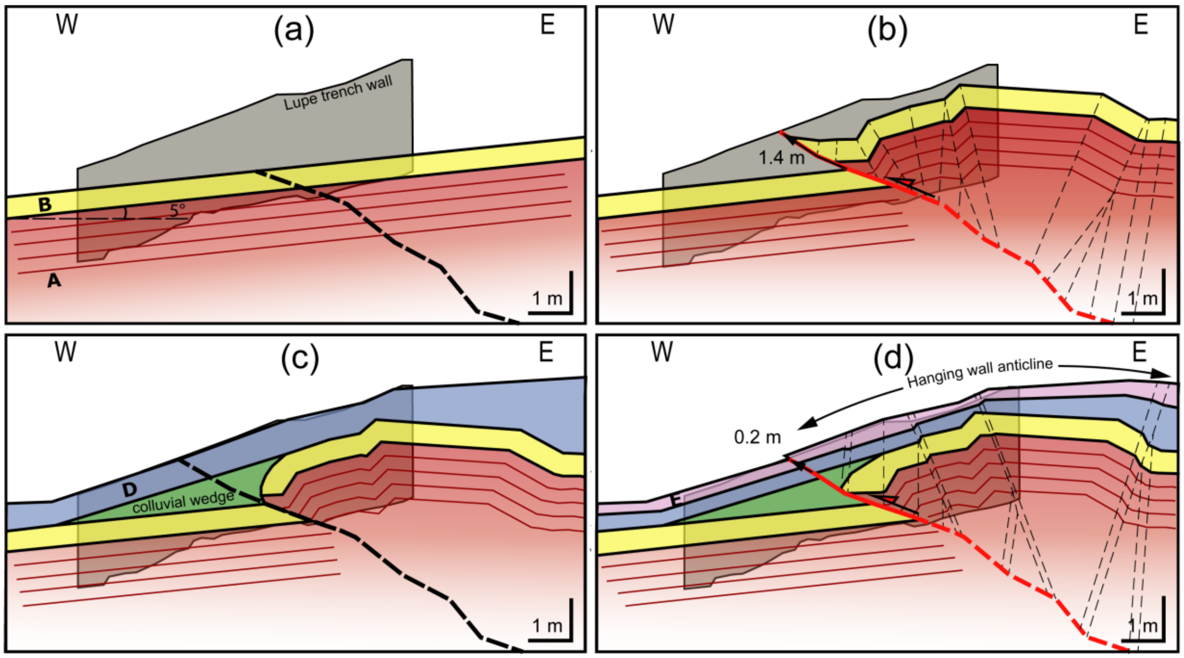

Figure 7. Kinematic modelling of the deformation observed at Lupe trench site. **(a)** Original slightly west-dipping alluvial deposits of Qe (units A and B). The black dashed line shows where the fault will develop in b). **(b)** First rupture of the Mesamávida fault displaces units A and B 1.4 m and folds them into an anticline in the hanging wall. **(c)** The scarp collapses forming a colluvial wedge (unit C). These units are covered later by alluvial deposition of unit D over the scarp**. (d)** Soil development on unit D results in a B horizon developing in unit D and the overlying A horizon of unit E. Finally, all units are displaced 0.2 m by a second rupture along the fault zone, and the hanging-wall anticline grows.

4.2. Barros Trench

Mapped units in the north wall of the Barros trench are labelled A to E from older to younger (Fig. 8). Unit A, at the base of the trench, is a ~0.2 m thick, matrix-supported and coarse-grained conglomerate, with ≤45% cobbles (Fig. 8c). The unit is poorly stratified with some pebble-rich beds. Unit B is a lens-shaped unit interbedded between units A and C and contains three subunits (Fig.8c). Subunit B1 is a 0.15-m-thick, fine-grained and well-sorted conglomerate (≤30% pebbles) with crossbedding at its base. Subunit B2 is a 0.38-m-thick, clay-rich crossbedded sand lens with ≤3% pebbles. Subunit B3 is a 0.21-m-thick, well-sorted, poorly stratified conglomerate (≤40% pebbles). Unit B’s upper contact with unit C is predominantly planar to slightly wavy. The three subunits of unit C include: subunit C1, a 0.37-m-thick bed of matrix-supported and well-sorted coarse-grained conglomerate (≤36% cobbles); subunit C2, a 0.32-m-thick, massive conglomerate with ≤25% boulders; and subunit C3, a fine gravel bed with ≤28% pebbles. In the western part of the trench, two stacked, westward tapering and wedge-shaped units were mapped as units D1 and D2 (Fig. 8c). The lower one (unit D1) is 0.27 m thick and consists of a bed with a chaotic fabric of clasts over a sub-horizontal bed of pebbles. The upper unit (unit D2) is 0.18 m thick, with a chaotic coarse-clast fabric in its eastern half, and west-tilted clasts in its western half. The matrix of this unit is darker than that of unit D1. We interpret units D1 and D2 as colluvium deposits. The uppermost unit (E) is a 0.2-0.61 m-thick, very loose, matrix-supported gravel. Its matrix is brown to dark brown, indicating organic-rich content, and is very irregular. These characteristics indicate that an A soil horizon has developed on it.

Structures in the center of the Barros trench consist of two subtle west-verging thrusts, referred to as western and eastern thrusts, and an east-verging deformation band (Figs. 8b-c). These structures show clast rotation, bed offsets, and folding of beds (Fig. 9). The ~30°E dipping, west-verging thrusts drive offset of units A to C. Abundant rotated and fractured clasts lie close to the thrust faults, with an eastward inclination of 45 ± 10°. The east-verging deformation band drives folding in the sand lens of unit B (Fig. 8c). This unit exhibits abundant evidence of liquefaction within this band, consisting of ball and pillow structures, nodules, sills, sedimentary dikes, and flames (Figs. 8c & 9c-d). The top of the sand lens (Unit B) is offset ~0.75 by the east verging deformation band, close to the bed offset along the western thrust. The overlying unit C is also deformed by this band, but its degree of deformation is reduced towards the surface. In the context of this thrusts-west-dipping deformation band configuration, we interpret that the latter is similar to a kink band shear zone. This configuration suggests a flat-ramp geometry for the faults a few meters beneath the trench floor, where these diverging structures are rooted (Fig. 10).

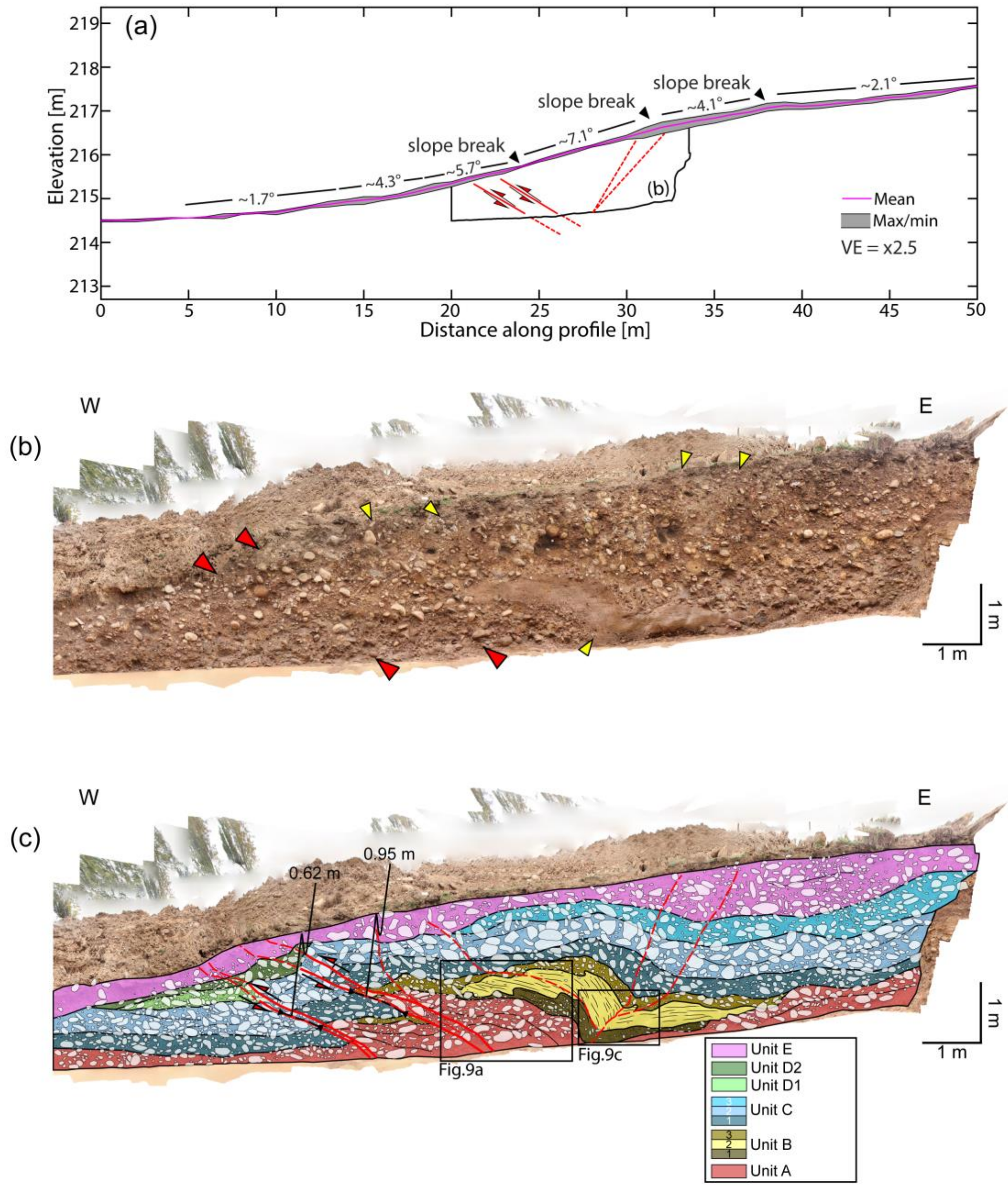

Figure 8. Logging of the Barros trench. **(a)** Topographic swath profile at the Barros trench site (5 m wide). The black lines depict the excavation, and the red lines trace the faults. Note the slope breaks along the profile above the faults and the kink band. **(b)** Photomosaic of the northern wall of the trench. Red and yellow triangles indicate end points of the trace of the main fault zone and related fractures, respectively. **(c)** Trench wall with labeled units (described in text), red lines mark fractures and the fault zone. The rectangles are the close-ups shown in Fig. 9.

As in the Lupe Trench, the west verging thrusts at the base of the scarp in the Barros trench suggest young, reverse surface-faulting. Slope breaks occur directly above the east-vergent deformation band and west-vergent faults (Fig. 8a). The main evidence for paleoearthquakes in this trench is given by the liquefaction structures and the occurrence of two stacked colluvium (Fig. 8c); these latter, considering the position of the logged thrusts, are interpreted as westward tapering colluvial wedges formed by collapse of the upper scarp following surface ruptures. Two paleoearthquakes are inferred. The first surface-faulting event, along the western thrust, offset ~0.62 m units A and C1-3 and promoted the accumulation of the colluvial deposit of Unit D1. The second faulting event- along the eastern thrust- offset ~0.95 m units A, B3 and C1-3 and caused the accumulation of the colluvial deposit of Unit D2. The western thrust was not activated during this second event and units D1 and D2, are not apparently displaced. Furthermore, Unit E is not displaced and hence corresponds to a post-faulting deposit.

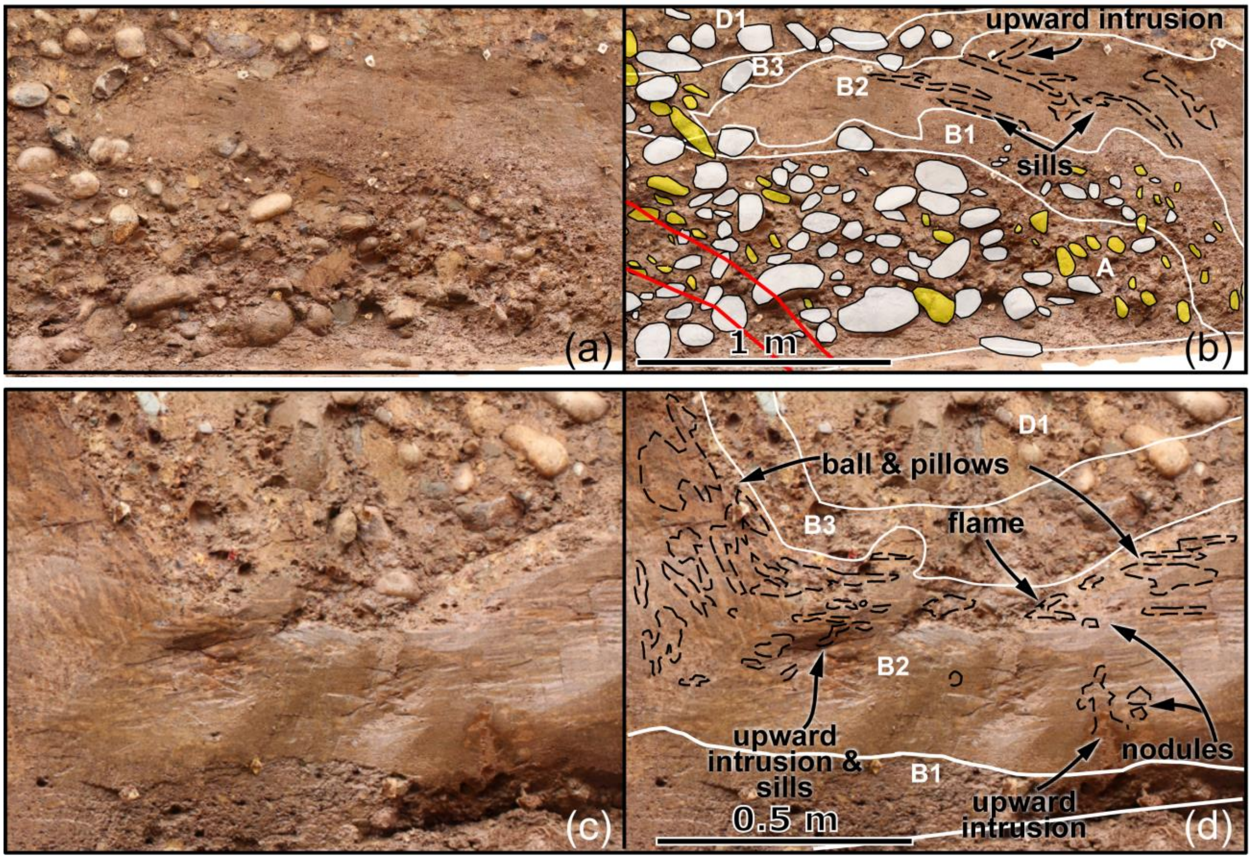

Figure 9. Close-ups to the liquefaction and tectonic features mapped in Lupe trench. **(a -b)** Eastern fault along the Barros trench wall and related liquefaction structures (black dashed lines); yellow clasts have been rotated within and close to the fault zone. The red thick line shows the fault zone **(c-d)** West-dipping kink band and related liquefaction structures (black dashed lines).

Based on our geometrical forward modelling (fault parallel flow), the mapped trench wall is consistent with surface faulting along two west-verging thrusts connected at ~3 m below the trench floor (Fig. 10). We begin with undeformed, sub-horizontal gravel units (Fig. 10a). The western reverse thrust fault slips ~0.6 m during a large earthquake, deforming units A to C, with the tip of the thrust in the hanging wall collapsing to form a debris-covered scarp (Fig. 10b). During the earthquake, antithetic deformation bands develop in the hanging wall, deforming units A to C (Fig. 10b). Subsequently, the scarp eroded leading to the accumulation of the upper part of the unit D1 colluvium (Fig.10c). The eastern reverse thrust fault slips ~0.9 m during a second large earthquake offsetting units A to C again (Fig. 10d). The tip of the eastern thrust in the hanging wall collapsed to form a second basal colluvial wedge followed by the accumulation of slope colluvium forming the upper part of unit D2 (Fig.10e). The entire scarp is then covered by alluvial unit E, which is not displaced (Fig. 10f). Soil development on unit E follows.

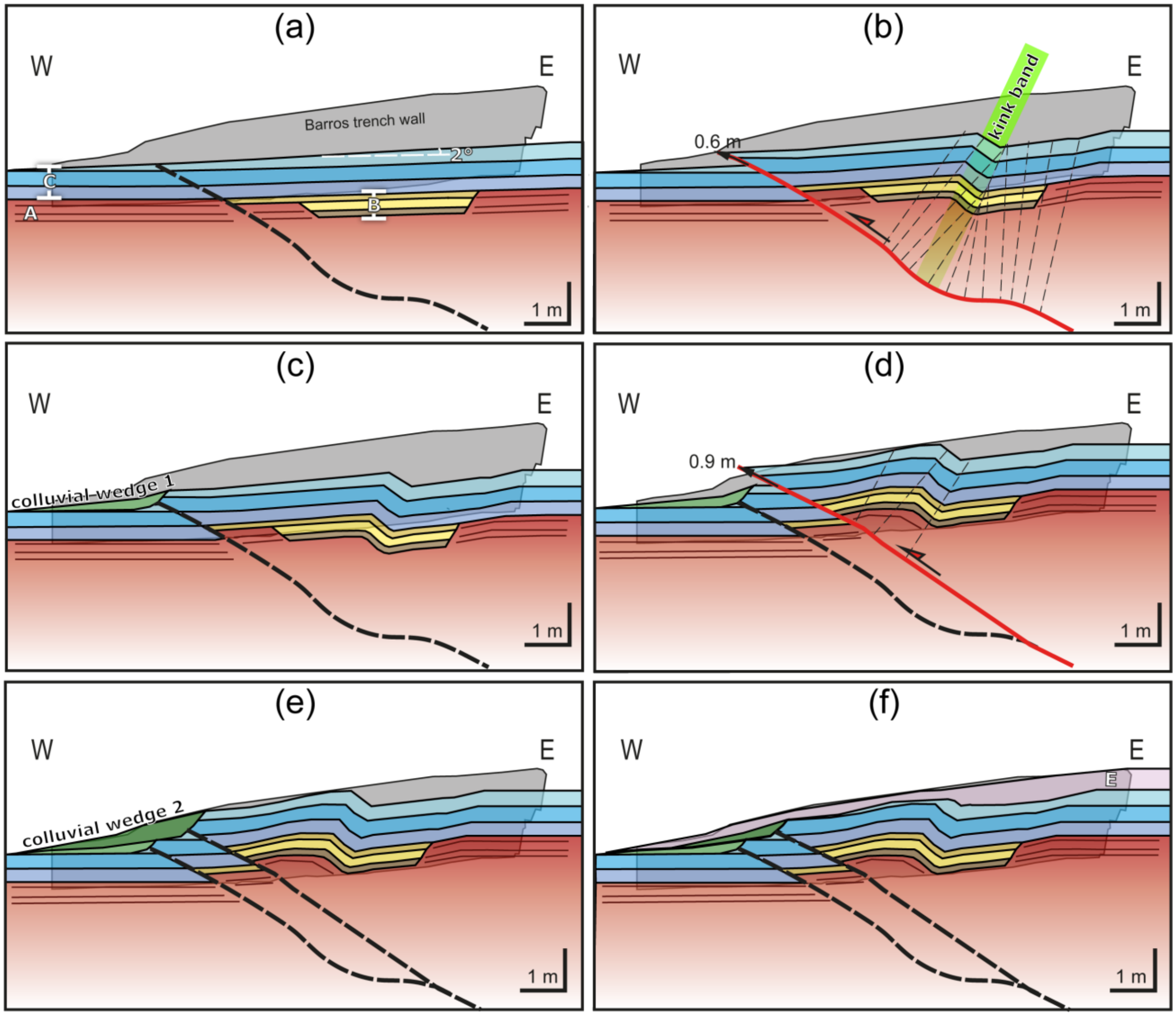

Figure 10. Kinematic modelling of the deformation observed at the Barros trench site. **(a)** Original slightly west-dipping alluvial deposits of Qe (units A, B, and D). The black dashed line corresponds to the trace of the future Mesamávida Fault. **(b)** First rupture of the Mesamávida Fault displaces units 0.6 m. **(c)** The scarp collapses, forming a first colluvial wedge in the hanging wall (unit D1). **(d)** A second rupture displaces units by 0.9 m along a second fault. The resulting hanging wall geometry requires a shallow ramp-flat-ramp geometry for this fault. **(e)** The hanging wall collapses, creating a second colluvial wedge (unit D2). **(f)** The deposition of unit E is followed by soil development; unit E is not deformed.

5. Morphotectonic analysis of the Mesamávida fault scarp

5.1. Vertical offset analysis

We analyze vertical offset along the scarp to assess how our conclusions from the trench sites about two Holocene surface-faulting earthquakes relate to the whole length of the Mesamávida fault scarp (Fig. 11). For this, we extracted 118 orthogonal-to-the-scarp topographic profiles from the 1-m-resolution LIDAR DTM, following the methods of Wei et al. (2019) and applying a MATLAB script by Colavitto et al. (2021). Profiles, each ≤110 m long, were traced using ArcGIS at sites along the scarp free of apparent fluvial erosion and/or human disturbance. Then at each profile site, the vertical offset was measured at the scarp midpoint using the hanging wall and the footwall far-field slopes (Figs. 11b-c). The vertical offset was measured three times and then averaged for each profile. We further restricted offsets by applying two quality measures: (1) profiles where slopes differed by >1° after repeated assessments were excluded because the slope differences may have been caused by erosion or other processes; and (2) profiles showing >10% variation in measurements or with uncertainties near the average offset value were discarded. Only 82 vertical offsets from the 118 profiles met these requirements and were used in the analysis (Figs. 11a-d).

The 82 vertical offsets along the Mesamávida scarp range between 0.7 and 8.7 m (Figs. 11c & S1 of Supporting Information 2). Maximum and minimum values of >6 m <2 m occur at ~1000 m and ~4000 m, and ~500 m and~ 3000 m from its northern end, respectively. Vertical offsets ranging between 2 and 6 m are concentrated in the central section of the scarp, between ~2000 m and ~5000 m from the northern end (Figs. 11a & 11c). We applied a statistical analysis, the Elbow Method (Figs. S2 & S3, Supporting Information 2), to determine an optimal number of three clusters of offsets. Then, we used the algorithm HDBSCAN (McInnes et al., 2017) identify each cluster's most representative value, resulting in peaks at ~1.15 m, ~3.6 m, and ~7.07 m of offset.

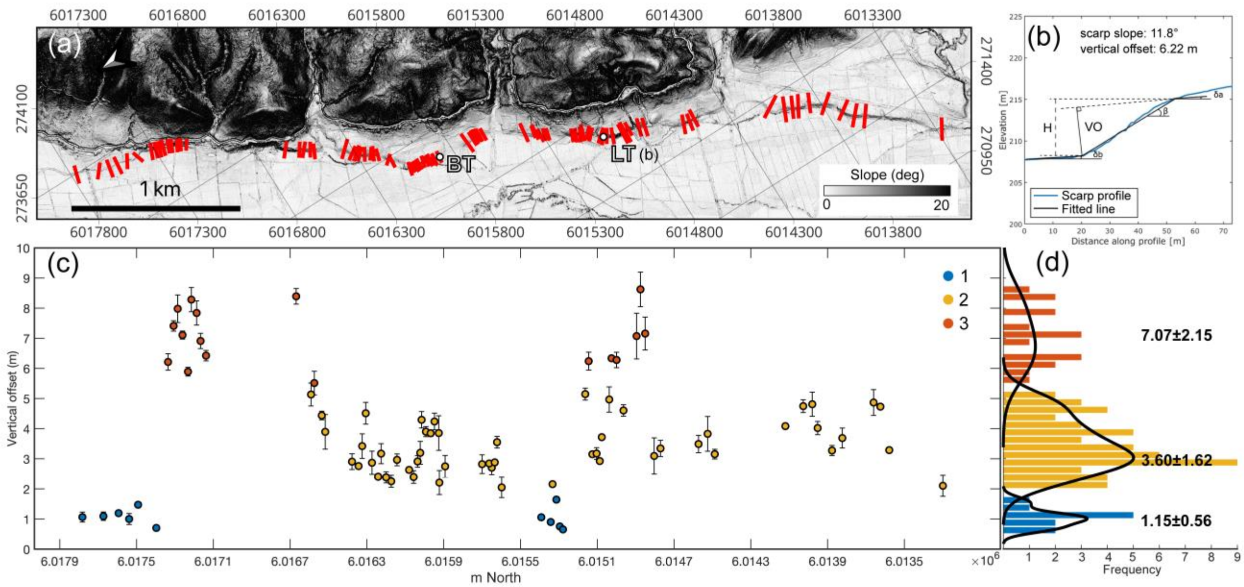

Figure 11. Quantification of the vertical offsets along the Mesamávida fault scarp. **(a)** Slope map depicting the location of the 82 topographic profiles along the Mesamávida scarp. **(b)** Example of how vertical offset is computed (at the Lupe trench site). **(c)** Along-strike distribution of vertical offset values from the profiles, colored circles identify the profiles in the three clusters. (**d)** Frequency distributions for the three clusters, mean, and one standard deviation error are given for each cluster (bin size = 0.2).

5.2. Morphological scarp dating

Along sections of the scarp where vertical offset analysis suggests a single surface rupture (lowest cluster, Fig. 11), we performed semi-automated morphological scarp dating using the Scarplet tool (Sare et al., 2019, Fig. 12). This method analyzes scarps in high-resolution (≤2 m/pixel) topographic datasets. Its performance is optimum in areas with smooth surrounding topography, minimal orientation changes of the scarp, and no other nearby linear features (Sare & Hilley, 2018). Using a two-dimensional windowed template function, the tool evaluates the curvature of a scarp, i.e., how much the scarp shape deviates from a straight-line shape. The window size used depends on (1) the suspected morphological age of the scarp (across-scarp length), which is defined by the function describing the change in the scarp curvature in the across-profile direction over time (Hilley et al., 2010), and (2) the out-of-profile distance (along-scarp length), which depends on the scarp length. However, if no morphological age is assumed, these parameters can be left unspecified, and the scarp curvature is assessed using a wide range of morphological ages (0 to 3000 m2; Sare & Hilley, 2018).

For the scarps that Scarplet detects it quantifies at each pixel the height (A), orientation (θ), signal-to-noise ratio (SNR; i.e., the ratio of the squared height A to the norm of the misfit template at each pixel) and morphological age of the scarp (Sare et al., 2019) (Figs. S4-S5 & Tables S1-S2, Supporting Information 2). False positives can be filtered using threshold values for SNR values, the scarp orientation, and amplitudes. The threshold for the different parameters depends on the characteristics of each analyzed scarp segment, but ranges are SNR <4-15, $\theta \geq 15°$, and $A > 2.5$ m. The final step in the analysis gathers maximum SNR pixels along-strike to produce a best linear estimate of scarp height and age (Sare et al., 2019). Because non-tectonic features, such as roads and channels, may appear in the filtered results, we made a final visual inspection to remove them manually (e.g., Sare et al., 2019). Only pixels on the scarp trace were considered for our morphological ages.

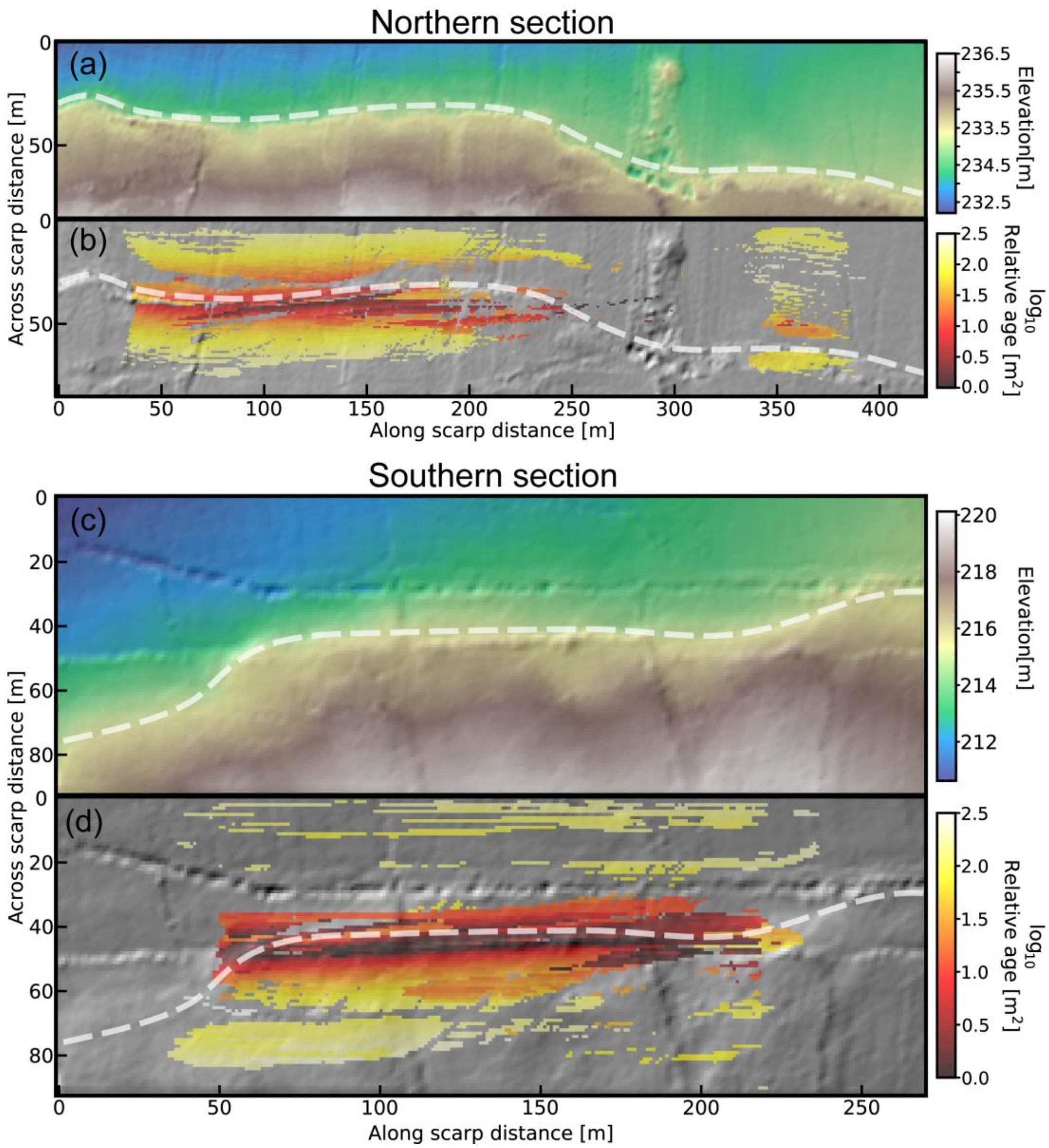

Figure 12. Semi-automated morphological dating of the Mesamávida fault scarp. **(a)** Northern segment of the Mesamávida scarp selected for morphologic dating analysis. **(b)** Resulting distribution of morphological relative ages for (a). **(c)** Southern segment of the Mesamávida scarp selected for morphologic dating analysis. **(d)** Resulting distribution of morphological relative ages. Dashed white lines define the base of the scarp.

Our morphological ages are illustrated in Fig. 12 and Fig. 13. For the selected scarp sections (Figs. 12a & 12c), relative ages are mostly derived from N-S striking portions (red and yellow zones in Figs. 12b & 12d). Values of amplitude and relative age show high variability along-strike but are positively correlated (Fig.13). Frequency distributions of relative ages range from $\log_{10}(0–2.5)$ m^2 (Figs. 13c &13f). Values inside the interquartile range were chosen as the morphological age for each segment (insets in Figs. 13c &13f). The resulting morphological ages span 1.58 to 50.12 m^2, with slightly higher values along the northern section of the scarp.

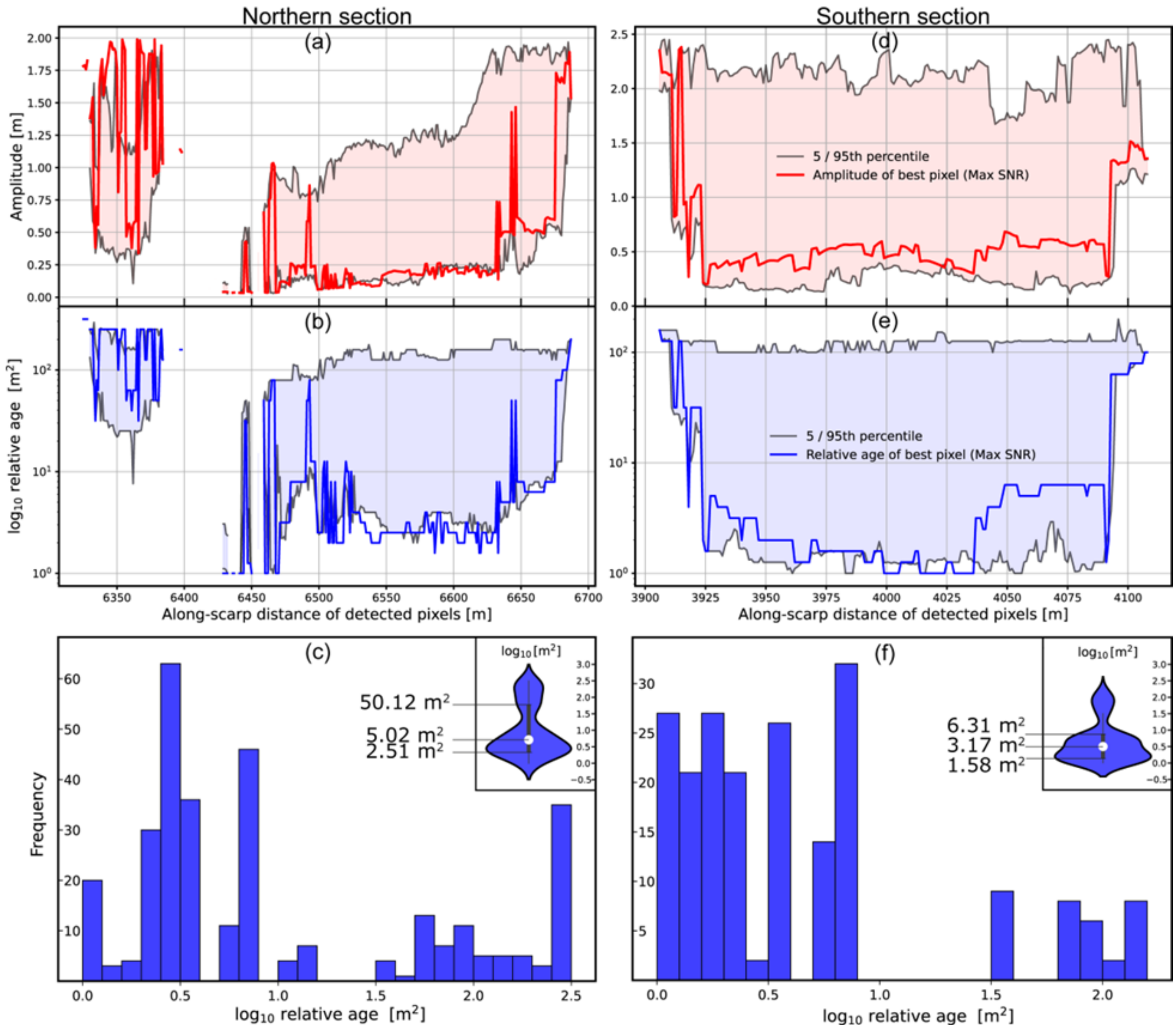

Figure 13. Outcome of the semi-automated morphological dating of the Mesamávida fault scarp. **(a)** Distribution of amplitudes, and **(b)** morphological ages of pixels along the northern section of the Mesamávida scarp. **(c)** Histogram and violin plot (inset) showing the distribution of morphological ages and how they cluster. **(d)** Distribution of amplitudes, and **(e)** morphological ages of pixels along the southern section of the Mesamávida scarp. **(f)** Histogram and violin plot (inset) showing the distribution of morphological ages and how they cluster.

6. Instrumental seismicity

To detect shallow crustal seismicity in the area, a temporary network of 12 seismic stations was deployed between July 2020 and January 2021 (Fig. 14). Each station contained a Lenartz 3Dlite Mk III short-period seismometer and a DiGOS DATA-CUBE3. A standard manual detection procedure identified 3001 earthquakes, however most of them with a very high instrumental gap. Following criteria used in similar studies (Bai et al., 2006; Sielfeld et al., 2019), we selected best quality earthquakes as those characterized by: (1) data registered by at least four stations, (2) clear detectable P and S waves arrivals, (3) an RMS ≤ 0.5, and 4) an azimuthal GAP ≤ 180°. A total of 56 high-quality events meet these criteria (Table S4, Supporting Information 2). These events were used to create a minimum 1D velocity model in VELEST (Kissling et al., 1995) which was then utilized to relocate the detected local seismicity. Of the relocated events, 24 were classified as crustal earthquakes (Fig. 14a), with hypocenters shallower than 40 km, consistent with the estimated Moho depth beneath the Mesamávida area (Tassara & Echaurren, 2012). All these events have very low local magnitudes (Ml between -1.5 and 0).

We compared seismicity to the crustal yield strength in a W-E profile computed following the procedure described by Giambiagi et al. (2022) (Fig. 14b). Local events detected by our network form two clusters located at distinct depth ranges (white triangles in Fig. 14b). A shallower cluster (10-25 km depth), with a roughly subvertical to slightly E-dipping orientation underneath the surface expression of the Mesamávida Fault, occurs entirely in an area of high background strength where seismic deformation is only possible along pre-existing fault planes. We also note that more abundant seismicity registered by CSN and OVDAS at upper crustal levels tends to concentrate at the boundary between high and low strength zones, but 50 km eastwards, coinciding with the structurally controlled axis of the volcanic front (Fig. 14b). The deeper (~40 km depth) cluster located by our network occurs underneath the zone of high crustal strength and close to the Moho. It is therefore likely related to stress concentration at the base of the crust.

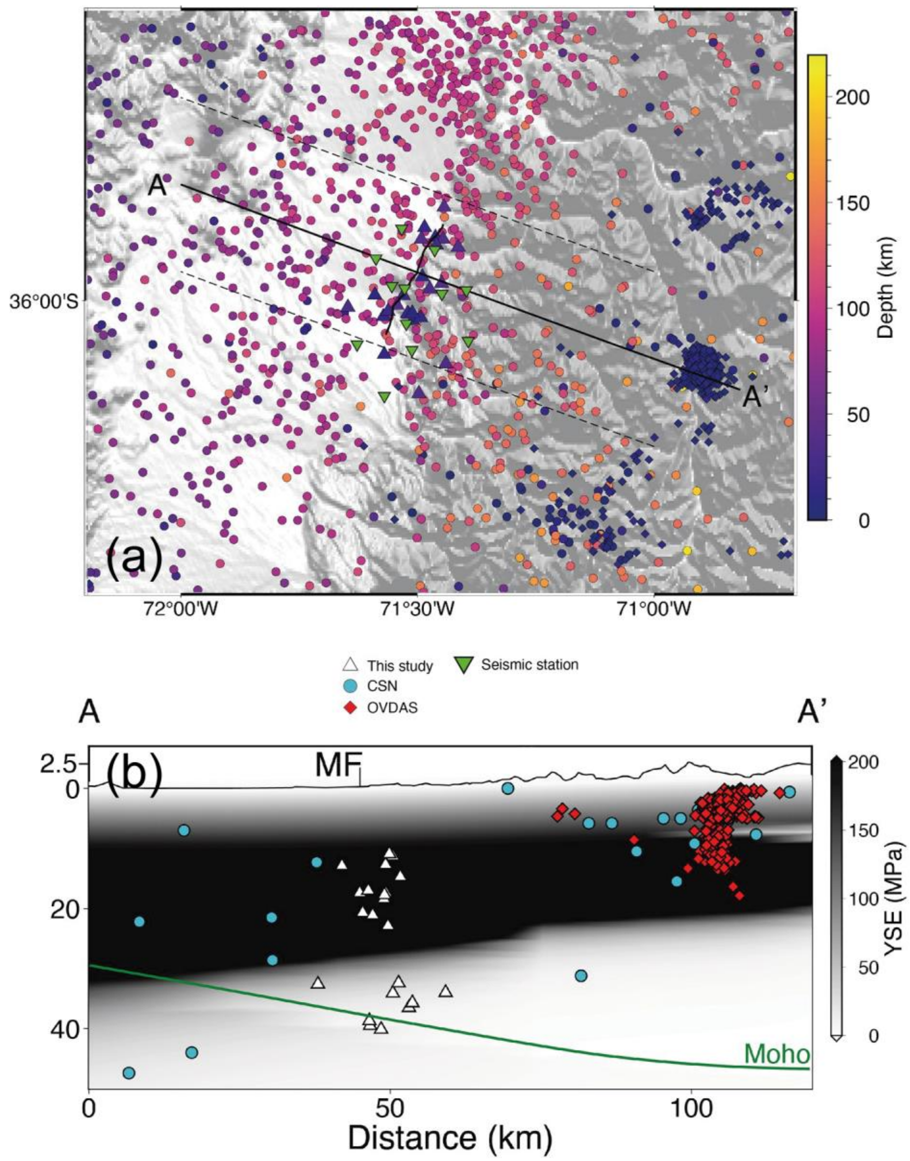

Figure 14. Instumental microseismicity within the study area. (a) Microseismicity recorded around the Mesamávida fault (triangles), by the Chilean National Seismological Center (CSN) network (circles) and by the Chilean volcanic monitoring service (OVDAS) network (diamonds); **(b)** AA' profile showing the distribution of microseismicity across the Mesamávida fault, along with the yield strength envelope of Giambiagi et al. (2022). White triangles: Events located by our local network; light blue circles: events by CSN network; red diamonds: events by OVDAS network.

7. Discussion

7.1. Pliocene-Quaternary deformation in the WATS at 36°S

Although no major faults have been mapped at the mountain front's base, both direct and indirect evidence suggest that the front along the boundary between the Central Valley and the Principal Cordillera at 36ºS has been structurally controlled by WATS branch faults since at least the Pliocene. The reverse fault exposed across the Achibueno River valley (Figs. 2a-c), the position of uplifted PQrm fluvial-alluvial deposits (Figs. 2a, 2e & 2g), and the steepness of the mountain front (Fig. 2f) support this inference. This inference is in line with the results of morphometric analysis by Oviedo-Reyes et al. (2024), which suggests moderate Quaternary tectonic deformation for this segment of the Central Valley-Principal Cordillera boundary. Pliocene-Quaternary faults of the WATS have also been mapped in longitudinally equivalent areas north and south of our study area (Farías et al., 2005; Hoke et al., 2007; Isacks, 1988; Riesner et al., 2018; Rojas Vera et al., 2014). For instance, Riesner et al. (2018) suggest that branches of the WATS (Armijo et al., 2010) at 33.5°S have driven the uplift of the Principal Cordillera over the last 25 Ma. At 37°S, Radic (2010) and Rojas Vera et al. (2014) show an inverted reverse fault which deforms Oligocene to Miocene volcanic rocks, along the western part of the Principal Cordillera (Fig. 1c).

We also infer from our mapping and topographic analysis that the main mountain front at 36ºS consists of structures that are growing northward; in the swath profile of Fig. 2e, the front progressively increases in height from south to north until the Achibueno River dissects it. The Mesamávida hill—particularly its western flank—shows a similar trend (Figs. 2g & 3a). The linearity of the western flank of the Mesamávida hill is anomalous in the Central Valley, which may indicate a secondary structure west of the main front (Fig. 2a). If so, the WATS in this area would be delineated by spatially related fault branches distributed across a ~10 km-wide zone, accommodating Pliocene–Quaternary deformation. In this context, the Mesamávida fault scarp may represent the most recent pulse of deformation along the WATS in this part of Chile. The crustal-scale interpretation of these structures and their role in the uplift of the western flank of the Andes is part of an ongoing debate. Armijo et al. (2010) and Riesner et al. (2017, 2018) suggest that they represent the frontal and most active faulting in a west-verging orogenic wedge. In contrast, Farías et al. (2010), Giambiagi et al. (2012, 2022), and Espinoza et al. (2024) propose that they are backthrusts associated with an east-verging crustal structure. Beyond this discrepancy, we propose that the Mesamávida fault is an active WATS branch in the area contributing to the uplift of the Andes.

7.2. Stratigraphic and paleoearthquake correlations

Based on the proximity of the trenches, stratigraphic characteristics and the relative position of the deposits, it is possible to correlate the exposed stratigraphic units as follows: Units A and B in the Lupe trench correlate, respectively, with Units A and C1–3 in the Los Barros trench (Figs. 5 & 8); the sand lens in the Los Barros trench (Unit B1-3) is a local stratigraphic feature that is not found in the Lupe trench. The colluvial wedge of Unit D1 in the Los Barros trench would then be equivalent to the colluvial wedge of Unit C1 in the Lupe trench (Figs. 5 & 8); this implies that the first paleoearthquake identified in both trenches corresponds to the same seismic event. In contrast, the colluvial wedge of Unit D2 in the Barros trench does not have an equivalent in the Lupe trench. Given the steeper slope of the scarp at the Lupe trench site, it is plausible that the second wedge was eroded prior to the deposition of Units D and E (Fig. 5). Consequently, if erosional and depositional regimes differ between the trench sites following the formation of the first colluvial wedge, younger stratigraphic units are difficult to correlate. Despite this, we infer that Unit D in the Lupe Trench can be correlated to Unit E in the Los Barros trench (Figs. 5 & 8); besides their stratigraphic similarities, both are the youngest deformed units in each trench. This correlation implies that the second paleoearthquake identified in both trenches also corresponds to the same seismic event. The proximity between the trench sites (approximately 1 km) and the magnitude of the interpreted coseismic slip, which empirically requires a rupture length of at least ~6 km (e.g., Thingbaijam et al. 2017; Fig. 15b-c), supports this interpretation.

7.3. Late Pleistocene-Holocene surface faulting along the Mesamávida fault

The stratigraphy and structures in the trenches across the Mesamávida scarp confirm that the scarp formed by surface faulting on west-verging (east-dipping) reverse faults at least twice after 14 ka (Figs. 5-10). However, the vertical component of fault offset measured across displaced alluvial units is much less than the scarp vertical offset in both trenches. In the Lupe trench, the ~1.06 m total measured fault offset is approximately one-sixth of the scarp vertical offset (~6.22 m). In the Barros trench, the ~1.57 m measured fault offset is also less than the vertical offset (~2.74 m). Our geometrical forward model accounts for these differences by developing a hanging wall anticline in the Lupe Trench and a west-dipping retro-shear deformation band in the Barros Trench site. These reveal sufficient folding in the hanging wall exposed in each trench to explain the scarp vertical offsets at the trench sites (Figs. 7 & 10). Alternatively, or complementarily, faults not exposed in the trench walls may accommodate deformation. Since deformation is often distributed in reverse fault zones (e.g., Cox et al., 2006; McCalpin & Carver, 2009), this possibility is reliable and would also explain why the scarp height is higher than the measured layer offsets.

By combining fault offsets of units in trenches with our geometrical modeling of folding and faulting, we explain apparent differences in fault slip per earthquake. In the Lupe trench, from the offsets recorded by the upper contact of unit B and the contact between units D and E (Fig. 5), we estimate minimum slips of 0.66 m and 0.2 m for the first and second earthquakes, respectively. When we apply our modeling to the Lupe trench stratigraphy the amounts of slip for these earthquakes are 1.4 m and 0.2 m. Although the unmodeled and modeled slip agree for the second earthquake, they differ for the first (0.66 m versus 1.4 m). We attribute the difference in slip for the first earthquake to: (1) in forward modeling (fault-bend folding) part of the slip is used to develop the folding; (2) modeling relies on a simplification of bed geometries that yields one of several non-unique solutions that try to match the present-day geometry and separation of units; (3) possible alluvial erosion of unit B (Fig. 5) would explain part of the lesser recorded slip during the first earthquake, and (4) during the first earthquake, most of the slip may have occurred on faults below the trench floor. In the Barros trench, from the offsets of units C1 and C2, slips of 0.95 m and 0.62 m were estimated for the first and second earthquakes, respectively. The palinpastic restoration for this trench suggests slip increments similar to those deduced from layer offsets in trenches. From this combined analysis, we propose that the coseismic slips interpreted for each paleoearthquake must be considered in the intervals defined by measured offsets and modelled slip increments.

When a fault produces successive surface ruptures along a scarp, fault offsets as expressed by scarp morphology tend to cluster into discrete groups, with each offset group corresponding to the cumulative slip during successive earthquakes (McGill & Sieh, 1991; Wei et al., 2019; Yeats et al., 1997). Based on the three clusters of vertical offsets along the Mesamávida scarp, we infer that the scarp was probably produced by at least three surface ruptures, even though only two were identified at the trench sites (scarp vertical offsets do not approach maximum values measured along the scarp at the trench sites). This discrepancy may be due to the trenches not being excavated deeply and long enough, or being located in areas where only two of the three Holocene earthquakes reached the surface.

Following the reasoning of Wei et al. (2019), we suggest that the peak vertical offset of ~1 m for the Mesamávida scarp is probably related to one, but not necessarily the most recent, single rupture. This value is about the same amount as the fault slips measured or modeled for individual earthquakes in the trenches (0.2-1.4 m). The remaining groups of vertical offsets therefore probably reflect the contribution of successive surface ruptures. Given the variable along-strike vertical offset distribution (Fig. 11c), we speculate that the slip during successive earthquakes at individual sites was variable, that different sections of the Mesamávida scarp ruptured during different earthquakes or that they present a variable degree of preservation. Despite the uncertainties in the coseismic offset estimates, the combined analysis of trench data, geometrical modeling, and scarp height measurements suggests that each earthquake along the Mesamávida Fault may involve slip of ca. 1 m.

To approach the age of the scarp, we have performed morphological dating for likely single-rupture scarp segments with the Scarplet code (Fig. 13). To derive numerical ages from our calculated morphological ages (Fig. 13), a k value is needed. Because a k value has not been determined for our study area, we apply values from areas with similar mean annual temperature and precipitation to central Chile at 36ºS: 11 m^2/ka (Hanks et al., 1984; Santa Cruz, California), 16 m^2/ka (Hanks et al., 1984; Raymond Fault, Pasadena, California), and 8.6 m^2/ka (Arrowsmith et al., 1998; Wallace Creek, California). Using these values of k, we calculate ages less than 3-6 ka for the Mesamávida scarp. We infer from these ages that a surface-faulting earthquake along the Mesamávida scarp, likely the most recent, occurred in the late Holocene. The Scarplet code was not explicitly developed for dating reverse fault scarps; therefore, our results must be interpreted cautiously. Nevertheless, since the calculated *kt* values correspond to approximately north-south oriented segments (Fig. 12). Given the absence of other nearby linear features in the landscape, the method is expected to yield reliable results (Sare & Hilley, 2018). The positive correlation between *kt* values and scarp amplitude suggests that the Scarplet approach provides reasonable estimates for the Mesamávida scarp. In addition, the morphological age assessment is validated by our OSL data, which provides a maximum age of approximately 14 ka for the Mesamávida scarp. Finally, and for comparison, morphological ages obtained for single-event scarp segments along the San Ramón reverse fault (33.5ºS; Fig. 1a), located in a similar climatic setting, using the diffusion model by Carretier et al. (2002), range between 5.5 and 20.13 ka (Rauld, 2011).

7.4. Present-day seismicity

The recorded crustal seismicity tends to define a NNE-striking and east-dipping cluster around the proposed Mesamávida fault trace (Fig. 14). Instrumental seismicity also seems to occur to the NNE and SSW of the Mesamávida fault scarp, perhaps suggesting that the Mesamávida fault is longer than its ~8-km Holocene scarp, reaching roughly 18 km in length. While our deployment confirms the presence of seismicity around the Mesamávida fault, quakes are scarce and of low magnitude, inhibiting strong inferences regarding fault geometry. Perhaps a longer recording time would allow for delineating the fault geometry and, in this way, demonstrate that it hosts seismicity nowadays. Despite these limitations and considering the relationship of micro-seismicity with the computed yield strength (Fig. 14b), we speculate that the recorded events can be attributed to a weak level – the Mesamávida fault –inside an otherwise high-strength upper crust. As also shown by Giambiagi et al (2022) at other latitudes along the Southern Central Andes, faults like this at the front of the main Andean cordillera tend to be rooted at depths of 20-30 km in regions of thermally reduced strength that act as detachment levels.

These inferences are consistent with similar studies of crustal seismicity and the structure of the WATS in the San Ramón fault area (Ammirati et al., 2019; Riesner et al., 2017). Despite working with data recorded by a dense seismic network, mainly close to the San Ramón fault trace, over several years, and using a deep-learning-based algorithm for P and S wave phases detection (Ammirati et al., 2019; 2022), authors were unable to locate events along the downdip prolongation of the WATS. The magnitude of completeness reported by Ammirati et al. (2022) is M1.5, much higher than the magnitudes we estimated. Most of the seismicity located by them seems to be related to structures eastward of the Cordilleran front, as also shown by us in our study region (Fig. 14b). This is consistent with the occurrence of large crustal earthquakes along the main cordilleran axis as shown by Comte et al. (2008) at 35ºS for a Mw 6.4 Earthquake in 2004, likely along the NNE striking dextral El Fierro Fault (Fig.1b). Moreover, Cardona et al. (2018) and Lupi & Miller (2014) report the occurrence, at 36°S, of a Mw 6.2 in 2012, probably linked to the NNE striking dextral El Melado fault.

7.5. Seismogenic potential and hazard

Our evidence shows that the Mesamávida fault has produced surface-rupturing earthquakes after 14ka and during the Holocene, indicating it is a capable fault (McCalpin, 2009). Earthquakes on capable faults are usually shallow, produce surface folding or faulting, and induce strong ground shaking (Comerci et al., 2013). At least six towns and cities with populations between 41.000 and 230.000 — some on unconsolidated deposits like those that the fault displaced at the trench site—occur within a radius of 60 km of the Mesamávida fault (Fig. 15a). Other critical facilities, for example the Colbún Dam, are located close to the fault (Fig. 1b). Thus, our results are a step forward in the appraisal of the seismic hazard posed by the WATS between 33ºS and 37ºS. Here, nine Quaternary faults associated with the Western Andean Thrust System (WATS) were mapped prior to this study (Fig. 15a). Only the San Ramón fault had previously published magnitude estimates based on field measured slip during Holocene earthquakes. In this work, we provide new estimates of fault slip—derived from trench stratigraphy and geometric modeling—for late Pleistocene-Holocene earthquakes on the Mesamávida fault. These estimates range from 0.6 to 1.4 m for the first paleoearthquake, and from 0.2 to 0.95 m for the second.

Given the available data, we cannot determine whether these values represent average or maximum coseismic displacements. Accordingly, we interpret them as local surface offsets. Despite this limitation, these data are useful for estimating moment magnitudes. To this end, we apply the empirical scaling relationships of Thingbaijam et al. (2017) and Thingbaijam & Mai (2020), which explicitly account for faulting style. The resulting moment magnitude estimates range between M5.6 and M7.06 (Fig. 15b).

Applying the same scaling relationships, we find that inferred coseismic slips >0.2 m imply rupture lengths greater than the length of the Mesamávida fault scarp. Although standard magnitude–scaling relationships may not fully apply to Chilean crustal earthquakes (e.g., 2004 Teno Earthquake; Comte et al., 2008), we interpret this inconsistency as the result of Late Quaternary scarp erosion by the Achibueno River and other drainages north of 36ºS (Fig. 2a). This interpretation is consistent with the subdued morphology of the mountain front marking the boundary between the Central Valley and the Principal Cordillera north of 36ºS, as described by Oviedo-Reyes et al. (2024). Therefore, it is likely that the preserved segment of the Mesamávida fault scarp—located between the Achibueno and Longaví rivers—represents only the southernmost extent of the inferred paleo-ruptures. This interpretation also agrees with the presence of a longer fault trace (~18 km) inferred from local microseismicity, and with the ~43 km total length proposed for the Mesamávida fault by Contreras et al. (2024).

To compare our trench-based magnitude estimates with those expected for the full extent of the rupture, we again use the scaling relations of Thingbaijam et al. (2017) and Thingbaijam & Mai (2020), considering rupture lengths of 8 km, 18 km, and 43 km—corresponding to the scarp length, the extent suggested by microseismicity, and the length mapped by Contreras et al. (2024), respectively. This yields moment magnitudes ranging from 5.87 to 7.05. From these, average slips of 0.6 m and 1.37 m can be inferred. Interestingly, these estimates—independent of our paleoseismic observations and geometrical modeling—are consistent with the slip values derived from the trench data (Fig. 15 b–c) and support our interpretation referred to coseismic slips of ca. 1m for each earthquake along the Mesamávida fault. The same approach was applied to the remaining nine WATS faults between 33°S and 37°S (Fig. 15b-c).

Despite uncertainties and the potential biases associated with the use of specific empirical relationships, our findings are consistent with previous estimates for other WATS faults, such as the San Ramón and Cariño Botado faults (Vargas et al., 2014; Estay et al., 2023). Ongoing efforts to refine the structural model of the region aim better to constrain the depth extent of the Mesamávida fault, thereby enabling more robust magnitude estimations. In the meantime, to be conservative, we propose a broad range of plausible moment magnitudes derived from the inferred coseismic surface offsets and the range of potential rupture lengths.

Two key parameters traditionally used to assess the seismic hazard of a fault are its slip rate and the recurrence interval of earthquakes (e.g., McCalpin, 2009). In this study, a significant limitation lies in the lack of precise chronological data to constrain the timing of deformation. However, the 14-ka age of the deposits in which the Mesamávida scarp formed, combined with the well-constrained scarp height, can be cautiously used to derive a rough slip rate. Considering the average scarp height of ~4.7 m, the OSL age, and a simplified fault dip of 35°E—consistent with trench observations—a slip rate of approximately 0.58 m/ka is obtained. Using the relationships between slip rate, magnitude, and recurrence interval proposed by Slemmons and Depolo (1986), we estimate recurrence intervals of about 400 years for ~M5.5 earthquakes and roughly 4,000 years for ~M7 events. These preliminary estimates for the Mesamávida fault are in line with those proposed for other WATS faults, such as the San Ramón and Cariño Botado faults.

Our findings highlight the seismic hazard posed by a newly discovered fault and enhance our understanding of the history of the WATS. The Mesamávida fault is only the third fault in this fault system with documented evidence of Holocene surface faulting. This discovery underscores the need for further neotectonic and paleoseismic surveys, especially in areas near the Central Valley–Principal Cordillera, where similar scarps in Quaternary — and possible Holocene — deposits occur. Expanding such studies north and south of our study area would provide critical information about the seismic hazard posed by the WATS and the Quaternary tectonics of the Andes.

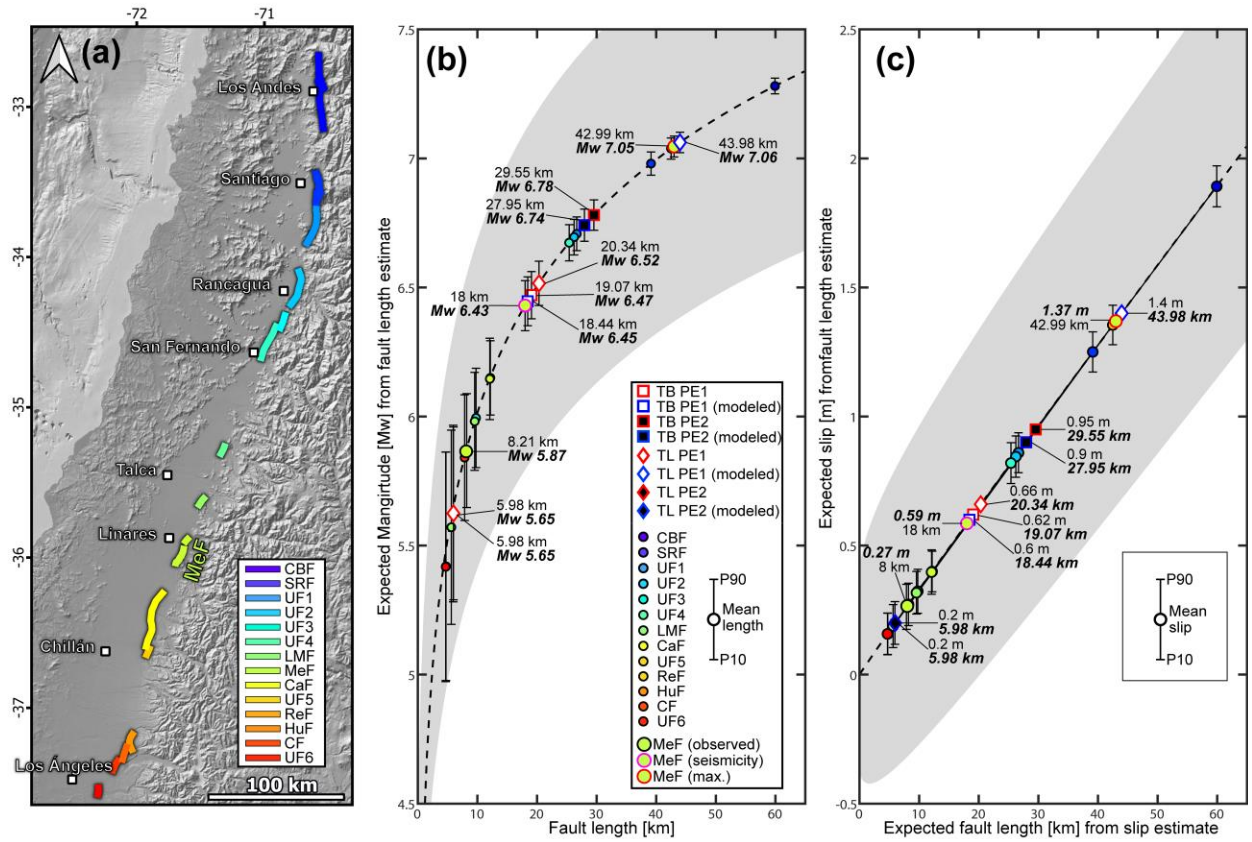

Figure 15. Self-consistent empirical relations for the faults along the WATS (32.5°-37.5°S) **(a)** Faults along the WATS between 32.5°S and 37.5°S (Maldonado et al., 2021). **(b)** Expected moment magnitudes and **(c)** Expected average slip per event from fault lengths estimation on WATS faults (Thingbaijam et al., 2017). Magnitudes for additional inferred earthquakes on the MeF extension are shown (8, 18, and ~43 km surface rupture lengths). Labeled values correspond to those related to the MeF. Squares and diamonds correspond to slip measurements from trench sites.

8. Conclusions

Our conclusions about the tectonic history of the border region of the Central Valley-Principal Cordillera at 36ºS from the Pliocene to the present are:

1) A hectometer-scale, N-S mountain front dominates the Principal Cordillera-Central Valley boundary. The steepness of the mountain front, uplifted Pliocene-Quaternary strata on its eastern edge, and a reverse fault that displaces Quaternary alluvium on the north side of the Achibueno River valley, provide evidence of tectonic deformation on fault branches of the Western Andean Thrust System (WATS) since at least the Pliocene.

2) The Mesamávida fault scarp, a metric-scale scarp in ~14-ka alluvium 200 m west of the main mountain front, was produced by Late Pleistocene to Holocene surface faulting and folding on the Mesamávida fault. Mapping of stratigraphy and structure in two trenches across the scarp, and geometric modelling of palinpastic restorations of faulting, suggest two earthquakes on west-verging reverse faults after ~14 ka. We highlight that stratigraphic and structural evidence for each of the two earthquakes is observed in both trenches. Fault slips during surface faulting were 0.2-1.4 m.

3) The vertical offset along the Mesamávida scarp ranges from 0.7 to 8.7 m but is heterogeneous along strike. Clusters of offsets with peaks at 1.15 m, 3.6 m, and 7.07 m were determined from statistical analyses of scarp morphology. We infer that the lowest peak represents slip during a single earthquake because the peak approximates slip during surface faulting measured in trenches and reconstructed with geometrical modelling.

4) Morphological scarp dating for inferred single-event scarp segments yields kt ages between 1.58 m^2 and 50.12 m^2. Despite the variability of kt values and the lack of a measured value for the study area, adopting k values determined for regions with similar precipitation and temperature suggests that the scarp records Holocene, and probably late Holocene, slip along the Mesamávida fault.

5) Microseismicity in the area is diffuse but denser near the trace of the Mesamávida fault. The relation between microseismicity and yield strength suggests that the fault extends to a depth of > 20 km.

6) From our study, it can be proposed that the Mesamávida fault is a capable fault (McCalpin, 2009). Estimates of fault slip—derived from trench stratigraphy, geometric modeling, and rupture length—for late Pleistocene-Holocene earthquakes on the Mesamávida fault, suggest that it can produce Mw 5.6-7.06 earthquakes. At least six cities of >41.000 people are within a radius of 60 km of the fault (Fig. 1b). We strongly recommend this fault be included as a potential source of large earthquakes in planning and mitigation designs for existing and new urban/industrial facilities in the region.

Acknowledgments

This research was financially supported by the Fondecyt Iniciación Project (11180509; JCA) and the Millenium Nucleus CYCLO. Forestal Arauco provided the LiDAR data. JCA is part of the CIMAsur interdisciplinary group at the University de Concepcion. FAA’s research is funded by ANID/FONDAP/15130015 and ANID/FONDAP/. JCA, FAA and MEV research are funded by the Anillo Project Salares. Postdoctoral research by LAS was funded by BecasChile (74220081) and by MEV by the ANID Fondecyt Postdoctorado 3200348. Our sincere gratitude goes to the dedicated individuals who participated in the field campaigns: Diego Molina, Camila Poblete, Diego Arias, Camila Oñate, Ignacio Huenupi, Javier Espinoza, Sebastián Cabrera, Nicolás Álvarez, and Nadia Jara. Additionally, we extend our heartfelt appreciation to local community members, including Miss Lupe, Don Manuel, Mister Cerda, and Mister Barros, whose invaluable assistance and warm hospitality were instrumental in successfully completing this work.

Open Research

All the included data- with the exception of the Lidar DTM- are available within the article or its supplementary materials. The employed codes are properly referenced.

References

Alvarado, P., & Beck, S. (2006). Source characterization of the San Juan (Argentina) crustal earthquakes of 15 January 1944 (MW 7.0) and 11 June 1952 (MW 6.8). *Earth and Planetary Science Letters*, *243*(3–4), 615–631.

Ammirati, J. B., Vargas, G., Rebolledo, S., Abrahami, R., Potin, B., Leyton, F., & Ruiz, S. (2019). The Crustal Seismicity of the Western Andean Thrust (Central Chile, 33°–34° S): Implications for Regional Tectonics and Seismic Hazard in the Santiago Area. *Bulletin of the Seismological Society of America*, *109*(5), 1985–1999. https://doi.org/10.1785/0120190082

Ammirati, J.-B., Villaseñor, A., Chevrot, S., Easton, G., Lehujeur, M., Ruiz, S., & Flores, M. C. (2022). Automated Earthquake Detection and Local Travel Time Tomography in the South-Central Andes (32–35° S): Implications for Regional Tectonics. *Journal of Geophysical Research: Solid Earth*, *127*(4), e2022JB024097.

Anderlini, L., Serpelloni, E., Tolomei, C., De Martini, P. M., Pezzo, G., Gualandi, A., & Spada, G. (2020). New insights into active tectonics and seismogenic potential of the Italian Southern Alps from vertical geodetic velocities. *Solid Earth Discussions*, *2020*, 1–27.

Armijo, R., Rauld, R., Thiele, R., Vargas, G., Campos, J., Lacassin, R., & Kausel, E. (2010). The West Andean Thrust, the San Ramón Fault, and the seismic hazard for Santiago, Chile. *Tectonics*, *29*(2), n/a-n/a. https://doi.org/10.1029/2008tc002427

Arriagada, D. (2021). *Paleosismología de la Falla Mesamávida: Análisis desde el mapeo de la Trinchera Crda Y Datación Morfológica de su escarpe a los 36°S, Región del Maule, Chile*. UNIVERSIDAD DE CONCEPCIÓN.

Arrowsmith, J. R., Rhodes, D. D., & Pollard, D. D. (1998). Morphologic dating of scarps formed by repeated slip events along the San Andreas Fault, Carrizo Plain, California. *Journal of Geophysical Research: Solid Earth*, *103*(5), 10141–10160. https://doi.org/10.1029/98jb00505

Bai, L., Wu, Z., Zhang, T., & Kawasaki, I. (2006). The effect of distribution of stations upon location error: Statistical tests based on the double-difference earthquake location algorithm and the bootstrap method. *Earth, Planets and Space*, *58*, e9–e12.

Burchfiel, B. C., Royden, L. H., der Hilst, R. D., Hager, B. H., Chen, Z., King, R. W., Li, C., Lü, J., Yao, H., & Kirby, E. (2008). A geological and geophysical context for the Wenchuan earthquake of 12 May 2008, Sichuan, People's Republic of China. *GSA Today*, *18*(7), 4–11.

Cardona, C., Tassara, A., Gil-Cruz, F., Lara, L., Morales, S., Kohler, P., & Franco, L. (2018). Crustal seismicity associated to rpid surface uplift at Laguna del Maule Volcanic Complex, Southern Volcanic Zone of the Andes. *Journal of Volcanology and Geothermal Research*, *353*, 83–94.

Carretier, S., Lucazeau, F., Ritz, J.-F., & Philip, H. (2002). Comparison of morphological dating models for cumulative reverse fault scarps. *Journal of Geophysical Research: Solid Earth*, *107*(B10), ETG–4.

Cheloni, D., Famiglietti, N. A., Tolomei, C., Caputo, R., & Vicari, A. (2024). The 8 September 2023, MW 6.8, Morocco earthquake: A deep transpressive faulting along the active high Atlas mountain belt. *Geophysical Research Letters*, *51*(2), e2023GL106992.

Colavitto, B., Alcacer, J. M., Rothis, M., Haro, F., Blanc, P. A., Onorato, R., & Perucca, L. (2021). Análisis paleosismológico de la falla Acequión mediante perfiles topográficos de escarpa (Precordillera de San Juan, Argentina). *Boletín de La Sociedad Geológica Mexicana*, *73*(2).

Comerci, V., Blumetti, A. M., Brustia, E., Di Manna, P., Guerrieri, L., Lucarini, M., & Vittori, E. (2013). Landslides Induced by the 1908 Southern Calabria: Messina Earthquake (Southern

Italy). In *Landslide Science and Practice: Volume 5: Complex Environment* (pp. 261–267). Springer.

Comte, D., Farías, M., Charrier, R., & González, A. (2008). Active tectonics in the Central Chilean Andes: 3D tomography based on the aftershock sequence of the 28 August 2004 shallow crustal earthquake. *International Symposium on Andean Geodynamics (ISAG 2008, Nice)*, *7*, 160–163.

Contreras, J., Escribano, J., Sepúlveda, F., & de la Cruz, R. (2024). *Geología del área San Clemente-Melado, región del Maule*.

Costa, C., Machette, M. N., Dart, R., Bast\'\ias, H., Paredes, J., Perucca, L., Tello, G., & Haller, K. (2000). Map and database of Quaternary faults and folds in Argentina. *US Geological Survey Open-File Report*, *108*, 75.

Cox, R. T., Cherryhomes, J., Harris, J. B., Larsen, D., Van Arsdale, R. B., & Forman, S. L. (2006). Paleoseismology of the southeastern Reelfoot Rift in western Tennessee and implications for intraplate fault zone evolution. *Tectonics*, *25*(3). https://doi.org/https://doi.org/10.1029/2005TC001829

Espinoza, M., Contreras, J., & Maksymowicz, A. (2024, November). Estructura y evolución geológica de la vertiente occidental de la Cordillera Principal en Chile Central (35.5°-36°S). *XXII Congreso Geológico Argentino*.

Estay, J., Pinto, L., Easton, G., De Pascale, G. P., Troncoso, M., Carretier, S., & Forman, S. L. (2023). Active thrust tectonics along the western slope of the Central Andes southernmost Pampean flat-slab segment (∼33°S, Chile): The Cariño Botado fault system. *Geomorphology*, *437*, 108801. https://doi.org/10.1016/j.geomorph.2023.108801

Estay, N. P., Yáñez, G., Carretier, S., Lira, E., & Maringue, J. (2016). Seismic hazard in low slip rate crustal faults, estimating the characteristic event and the most hazardous zone: study case San Ramón Fault, in southern Andes. *Natural Hazards and Earth System Sciences*, *16*(12), 2511–2528.

Farías, M., Charrier, R., Comte, D., Martinod, J., & Hérail, G. (2005). Late Cenozoic deformation and uplift of the western flank of the Altiplano: Evidence from the depositional, tectonic, and geomorphologic evolution and shallow seismic activity (northern Chile at 19°30′S). *Tectonics*, *24*(4). https://doi.org/10.1029/2004TC001667

Farías, M., Comte, D., Charrier, R., Martinod, J., David, C., Tassara, A., Tapia, F., & Fock, A. (2010). Crustal-scale structural architecture in central Chile based on seismicity and surface geology: Implications for Andean mountain building. *Tectonics*, *29*(3). https://doi.org/https://doi.org/10.1029/2009TC002480

Giambiagi, L., Mescua, J., Bechis, F., Tassara, A., & Hoke, G. (2012). Thrust belts of the southern Central Andes: Along-strike variations in shortening, topography, crustal geometry, and denudation. *GSA Bulletin*, *124*(7–8), 1339–1351. https://doi.org/10.1130/B30609.1

Giambiagi, L., Tassara, A., Echaurren, A., Julve, J., Quiroga, R., Barrionuevo, M., Liu, S., Echeverr\'\ia, I., Mardónez, D., Suriano, J., & others. (2022). Crustal anatomy and evolution of a subduction-related orogenic system: Insights from the Southern Central Andes (22-35 S). *Earth-Science Reviews*, *232*, 104138.

Hanks, T. C., Bucknam, R. C., Lajoie, K. R., & Wallace, R. E. (1984). Modification of wave-cut and faulting-controlled landforms. *Journal of Geophysical Research: Solid Earth*, *89*(B7), 5771–5790. https://doi.org/10.1029/JB089iB07p05771

Hauser, A. (1995). *Hoja Talca: Region VII*. Servicio Nacional de Geolog\'\ia y Miner\'\ia.

Hoke, G. D., Isacks, B. L., Jordan, T. E., Blanco, N., Tomlinson, A. J., & Ramezani, J. (2007). Geomorphic evidence for post-10 Ma uplift of the western flank of the central Andes 18°30′-22°S. *Tectonics*, *26*(5), n/a-n/a. https://doi.org/10.1029/2006TC002082

Isacks, B. L. (1988). Uplift of the central Andean Plateau and bending of the Bolivian Orocline. *Journal of Geophysical Research*, *93*(B4), 3211–3231. https://doi.org/10.1029/JB093iB04p03211

Karzulovic, J., & Hauser, A. (1979). *Edades K/Ar en rocas volcánicas e intrusivas del área de los proyectos hidroeléctricos Colbún-Machicura-Melado Empresa Nacional de Electricidad SA VII región*.

Kendrick, E., Brooks, B. A., Bevis, M., Smalley, R., Lauria, E., Araujo, M., & Parra, H. (2006). Active orogeny of the South-Central Andes studied with GPS geodesy. *Revista de La Asociación Geológica Argentina*, *61*(4), 555–566.

Kissling, E., Kradolfer, U., & Maurer, H. (1995). Program VELEST user's guide-Short Introduction. *Institute of Geophysics, ETH Zurich*.

Kübler, S., Friedrich, A. M., Gold, R. D., & Strecker, M. R. (2018). Historical coseismic surface deformation of fluvial gravel deposits, Schafberg fault, Lower Rhine Graben, Germany. *International Journal of Earth Sciences*, *107*, 571–585.

Lupi, M., & Miller, S. A. (2014). Short-lived tectonic switch mechanism for long-term pulses of volcanic activity after mega-thrust earthquakes. *Solid Earth*, *5*(1), 13–24.

Marliyani, G. I., Arrowsmith, J. R., & Whipple, K. X. (2016). Characterization of slow slip rate faults in humid areas: Cimandiri fault zone, Indonesia. *Journal of Geophysical Research: Earth Surface*, *121*(12), 2287–2308. https://doi.org/10.1002/2016JF003846

McCalpin, J. P. (2009). *Paleoseismology* (2nd ed., Vol. 95). International Geophysics Series.

McCalpin, J. P., & Carver, G. A. (2009). Chapter 5 Paleoseismology of Compressional Tectonic Environments. In *International Geophysics* (Vol. 95, pp. 315–419). Academic Press. https://doi.org/https://doi.org/10.1016/S0074-6142(09)95005-7

McCalpin, J. P., Ferrario, F., Figueiredo, P., Livio, F., Grützner, C., Pisarska-Jamroży, M., Quigley, M., Reicherter, K., Rockwell, T., Štěpanč\'\iková, P., & others. (2023). New developments in onshore paleoseismic methods, and their impact on Quaternary tectonic studies. *Quaternary International*, *664*, 59–76.

McGill, S. F., & Sieh, K. (1991). Surficial offsets on the central and eastern Garlock fault associated with prehistoric earthquakes. *Journal of Geophysical Research: Solid Earth*, *96*(B13), 21597–21621.

McInnes, L., Healy, J., Astels, S., & others. (2017). hdbscan: Hierarchical density based clustering. *J. Open Source Softw.*, *2*(11), 205.

Medwedeff, D. A., & Suppe, J. (1997). Multibend fault-bend folding. *Journal of Structural Geology*, *19*(3–4), 279–292.

Muñoz, J., & Niemeyer, H. (1984). *Hoja Laguna del Maule, Regiones del Maule y del B\'\io B\'\io*.

Oviedo-Reyes, J. A., Cortes-Aranda, J., & Fernández, A. (2024). Faulting Styles Imprinted on Geomorphic Features: Insights from Morphometric Analysis and Paleostress Tensors in the Western Andean Front (35° S–38° S), Chile. *Journal of South American Earth Sciences*, 105326.

Pathier, E., Fielding, E. J., Wright, T. J., Walker, R., Parsons, B. E., & Hensley, S. (2006). Displacement field and slip distribution of the 2005 Kashmir earthquake from SAR imagery. *Geophysical Research Letters*, *33*(20).

PE Limited. (2020). *MOVE Suite - Integrated Production Modelling software (IPM)*.

Radic, J. P. (2010). Las cuencas cenozoicas y su control en el volcanismo de los Complejos Nevados de Chillán y Copahue-Callaqui (Andes del Sur, 36-39 S). *Andean Geology*, *37*(1), 220–246.

Rauld, R. (2011). Deformación cortical y peligro sísmico asociado a la falla San Ramón en el frente cordillerano de Santiago, Chile Central (33 S). *Santiago, Chile: PhD. Thesis in Science of Geology, Universidad de Chile*.

Riesner, M., Lacassin, R., Simoes, M., Armijo, R., Rauld, R., & Vargas, G. (2017). Kinematics of the active West Andean fold-and-thrust belt (central Chile): Structure and long-term shortening rate. *Tectonics*, *36*(2), 287–303. https://doi.org/10.1002/2016TC004269

Riesner, M., Lacassin, R., Simoes, M., Carrizo, D., & Armijo, R. (2018). Revisiting the Crustal Structure and Kinematics of the Central Andes at 33.5°S: Implications for the Mechanics of Andean Mountain Building. *Tectonics*, *37*(5), 1347–1375. https://doi.org/10.1002/2017TC004513

Rockwell, T., Fonseca, J., Madden, C., Dawson, T., Owen, L. A., Vilanova, S., & Figueiredo, P. (2009). Palaeoseismology of the Vilariça segment of the Manteigas-Bragança fault in northeastern Portugal. *Geological Society, London, Special Publications*, *316*(1), 237–258.

Rockwell, T. K., Ragona, D. E., Meigs, A. J., Owen, L. A., Costa, C. H., & Ahumada, E. A. (2014). Inferring a thrust-related earthquake history from secondary faulting: A long rupture record of La Laja Fault, San Juan, Argentina. *Bulletin of the Seismological Society of America*, *104*(1), 269–284.

Rojas Vera, E. A., Folguera, A., Valcarce, G. Z., Bottesi, G., & Ramos, V. A. (2014). Structure and development of the Andean system between 36 and 39 S. *Journal of Geodynamics*, *73*, 34–52.

Sare, R., & Hilley, G. (2018). Scarplet: A Python package for topographic template matching and diffusion dating. *Journal of Open Source Software*, *3*(31), 1066. https://doi.org/10.21105/joss.01066

Sare, R., Hilley, G. E., & DeLong, S. B. (2019). Regional-Scale Detection of Fault Scarps and Other Tectonic Landforms: Examples From Northern California. *Journal of Geophysical Research: Solid Earth*, *124*(1), 1016–1035. https://doi.org/10.1029/2018JB016886

Schoenbohm, L., Costa, C., Brooks, B., Bohon, W., Gardini, C., & Cisneros, H. (2013). Fault interaction along the Central Andean thrust front: The Las Peñas thrust, Cerro Salinas thrust and the Montecito anticline. *AGU Fall Meeting Abstracts*, *2013*, T31D–2543.

Sepúlveda, T. (2019). *Neotectónica Y Paleosismología de la Falla Mesamávida: Evidencia de Actividad Cuaternaria Tardía del Cabalgamiento Andino Occidental (WATF) en la Región del Maule (36°S) , Chile Central*. Universidad de Concepción.

Sielfeld, G., Lange, D., & Cembrano, J. (2019). Intra-arc crustal seismicity: Seismotectonic implications for the southern Andes volcanic zone, Chile. *Tectonics*, *38*(2), 552–578.

Slemmons, D., & Depolo, C. (1986). Evaluation of active faulting and associated hazards. *Active Tectonics*, 45–62. https://books.google.es/books?hl=es&lr=&id=qaz9KnE2lxQC&oi=fnd&pg=PA45&dq=Slemmons+and+DePolo+1986&ots=MsCJibuxjQ&sig=SK3lJcFWe51HcA15rpy8hp-d2qg

Stein, R. S., & Yeats, R. S. (1989). Hidden earthquakes. *Scientific American*, *260*(6), 48–59.

Tassara, A., & Echaurren, A. (2012). Anatomy of the Andean subduction zone: three-dimensional density model upgraded and compared against global-scale models.

Geophysical Journal International, *189*(1), 161–168. https://doi.org/10.1111/J.1365-246X.2012.05397.X
Teloni, S., Invernizzi, C., Mazzoli, S., Pierantoni, P. P., & Spina, V. (2021). Seismogenic fault system of the Mw 6.4 November 2019 Albania earthquake: New insights into the structural architecture and active tectonic setting of the outer Albanides. *Journal of the Geological Society*, *178*(2), jgs2020–193.
Thingbaijam, K. K., & Mai, P. M. (2020). *Further Notes on the New Empirical Earthquake Source-Scaling Laws*.
Thingbaijam, K. K. S., Martin Mai, P., & Goda, K. (2017). New Empirical Earthquake Source-Scaling Laws. *Bulletin of the Seismological Society of America*, *107*(5), 2225–2246. https://doi.org/10.1785/0120170017
Uzarski, J., & Arnold, C. (2001). Chi-Chi, Taiwan, earthquake of September 21, 1999, reconnaissance report. *Earthquake Spectra*, *17*.
Vergara, M., Morata, D., Hickey-Vargas, R., Lopez-Escobar, L., & Beccar, I. (1999). Cenozoic tholeiitic volcanism in the Colbún area, Linares Precordillera, central Chile (35o35’-36oS). *Revista Geológica de Chile*, *26*(1), 23–41.
Wei, Z., He, H., Su, P., Zhuang, Q., & Sun, W. (2019). Investigating paleoseismicity using fault scarp morphology of the Dushanzi Reverse Fault in the northern Tian Shan, China. *Geomorphology*, *327*, 542–553.
Yang, Y.-H., Hu, J.-C., Chen, Q., Lei, X., Zhao, J., Li, W., Xu, R., & Chiu, C.-Y. (2021). Shallow slip of blind fault associated with the 2019 M S 6.0 Changning earthquake in fold-and-thrust belt in salt mines of Southeast Sichuan, China. *Geophysical Journal International*, *224*(2), 909–922.
Yeats, R. S., Sieh, K. E., & Allen, C. R. (1997). The geology of earthquakes. *(No Title)*.
Zapata, T. R., & Allmendinger, R. W. (1996). Thrust-front zone of the Precordillera, Argentina: a thick-skinned triangle zone. *AAPG Bulletin*, *80*(3), 359–381.